Title
Laser Induced Breakdown Spectroscopy and Applications Toward Thin Film Analysis

Author
Owens, Travis Nathan

Publication Date
2011

Peer reviewed|Thesis/dissertation

Laser Induced Breakdown Spectroscopy and Applications Toward Thin Film Analysis

by

Travis Nathan Owens

A dissertation submitted in partial satisfaction of the
requirements for the degree of
Doctor of Philosophy

in

Engineering-Mechanical Engineering

in the

Graduate Division

of the

University of California, Berkeley

Committee in charge:

Professor Costas Grigoropoulos, Chair
Professor Samuel Mao
Professor Michael Frenklach
Professor Ronald Gronsky

Fall 2011

Laser Induced Breakdown Spectroscopy and Applications Toward Thin Film Analysis

Abstract

Laser Induced Breakdown Spectroscopy and Applications Toward Thin Film Analysis

by

Travis Nathan Owens

Doctor of Philosophy in Engineering-Mechanical Engineering

University of California, Berkeley

Professor Costas Grigoropoulos, Chair

Laser induced breakdown spectroscopy (LIBS) provides the opportunity to analyze almost any element, from any material, in any environment. Among the many applications of LIBS is the analysis of thin films and multilayered structures. An automated system was designed and built to conduct LIBS using Nd:YAG and Ti:Sapphire lasers, broadband and high-resolution spectrometers and detectors. This system incorporates the sample manipulation as well as laser and spectrometer control and timing. A series of experiments were conducted to analyze the ability of nanosecond and femtosecond lasers to detect Mg impurities in thin TiO_2 films using LIBS. It was determined that optimal detection occurs early in the plasma ionic/atomic emission with detection capabilities in the parts-per-million range. Another series of experiments were conducted using LIBS to analyze thin transparent organic films, with specific emphasis on the effect of film thickness and interplay between film and substrate. The challenges of ablating and measuring multiple layers have also been explored using various laser wavelengths. The effectiveness of LIBS has been demonstrated for depth profiling of CIGS solar cells. Ablation crater and ablation threshold analysis aided in understanding and overcoming some of the obstacles in depth profiling. One of the challenges with LIBS is the identification and mitigation of matrix effects. This problem was explored using a Mg tracer element and various compositions of the suspected elements Si, Ca, and Sr which can cause errors in LIBS analysis. The goal of this dissertation is to investigate the ability of LIBS to conduct detailed thin film analysis for a variety of materials and potential applications. This includes analyzing trace elements from a traditionally noisy background, measuring difficult to ablate thin films, and the unique challenges associated with multilayered structures.

Contents

List of Figures

List of Tables

Acknowledgments

I am unable to fully express my extreme gratitude to Costas Grigoropoulos and Samuel Mao for giving me the opportunity to join the legacy of learning, research, growth, and fellowship that has become synonymous with The University of California at Berkeley. The experiences I've had are unparalleled and represent the epitome of academic research. I have had the honor to work both on campus and at Lawrence Berkeley National Lab. The guidance and trust these two men have shown me throughout my graduate career has been a true blessing. In every meeting or discussion I have always come away with renewed vigor and the drive to pursue new ideas and questions. I will always be indebted to my advisors and hope to maintain a fantastic working relationship with them both.

I would also like to thank Rick Russo for adopting me into his research group and sharing his experience, time, equipment and research facilities with me. His generosity and openness began a collaboration which transformed into an amazing working relationship. It has been a great privilege to work with David Hwang, Ming-Tsang Lee, Xianglei Mao, Jhanis Gonzalez, and Vassilia Zorba who have acted as my lab managers, collaborators, and research gurus. I am thankful not only for their help, but also for the ability to count them among my friends.

A successful research program is not possible without a fantastic group of colleagues, co-workers and lab-mates. I would like to thank Alexander Sherry, Angel Fernandez-bravo Del Olmo, Coleman Kronawitter, Daeho Lee, Dayana Oropeza, Derrick Speaks, Dongdong Wang, Erin Canfield, Eunpa Kim, Heng Pan, Hojeong Jeon, Inhee Choi, Jaewon Chung, Jake J.H. Yoo, Jungbin In, Ken Kim, Kenneth Russell Carrington, Lucas Oehlerking, Matt Beres, Matthew Rogers, Michael Fina, Mohamed Elmalatawy, Moosung Kim, Nipun Misra, Paola Vega, Sang Gil Ryu, Sanghoon Ahn, Seung Hwan Ko, Siv Hjorth Dundas, Steven Barcelo, Timothy Suen, Tony Ho, Xiaobo Chen, Xiaojun Zhang, and Yuan Lu.

A special thank you to my family whose support, faith, and guidance helped keep me grounded and strive to embody the ideals and morals I believe in. I'd like to thank my father who always believes in me and pushes me to believe in myself. To my mother who's love and comfort has gotten me through hard times, and who is incapable of finding fault in anything I do. I'd also like to thank my brother who has inspired me to work hard, learn as much as possible and question everything. No words can adequately express my gratitude to Shan Wang whose daily support, love, and friendship has made my life complete.

In closing I would like to thank my entire committee for providing their insight, experience, knowledge, suggestions and taking time to review this dissertation. In addition to my co-advisors, I am grateful to have the approval of Ronald Gronsky whose dedication to his students constantly surprises me. I would also like to thank Professor Frenklach, who has graciously agreed to help guide me with this dissertation and represents the thoughtful encouragement unique to Professors at U.C. Berkeley

Chapter 1

Introduction

1.1 Introduction to Laser Induced Breakdown Spectroscopy

Laser induced breakdown spectroscopy (LIBS) is generally regarded as the study of atomic and ionic emission from a laser generated plasma. This technique is also known as Laser Induced Plasma Spectroscopy (LIPS), and extends to the study of ultraviolet, visible, infrared radiation, and molecular vibration from excited species. The laser generated plasma serves as the source of ablation, vaporization, atomization and excitation of the sample in question. The majority of LIBS research has been done on solid samples, but the technique has also been applied to liquid, gas, and aerosol samples. In fact, LIBS can provide the unique chemical signature of any element, from any material, in any environment. LIBS has been successfully applied to analyze metal, ceramic, paint, soil, glass, bone, plants, powders, explosives, and polymers. It has been performed in atmospheric conditions, at the bottom of the ocean and on the barren landscape of Mars. There is no sample preparation required to conduct LIBS analysis and it can even be done remotely. These advantages make LIBS a potential solution for a wide variety of applications.

There are three major components to any LIBS apparatus: a laser, wavelength selector, and detector. The specific requirements for each component are flexible and depend solely on the desired measurement capabilities. Lasers used in LIBS can be continuous wave, pulsed, ultrafast, solid state, gas, or dye lasers. The wavelength selectors can be optical filters, prisms or gratings and the detection of LIBS emission can be captured on film, photomultipliers, or cameras.

Although the approach to chemical analysis with LIBS seems simplistic, the underlying fundamentals and many interconnected parameters make it very difficult to conduct detailed, quantitative, calibration-free measurements. The freedom to take many approaches with LIBS introduces the problem that each analysis is unique to the instrumentation with which it was made. The fundamental processes of laser ablation, plasma expansion and plasma emission are very complex individually, but become increasingly convoluted as they

are combined together. Despite these issues, LIBS is an excellent resource for chemical identification and analysis with the potential for an abundance of applications.

A Brief History of LIBS

Born immediately after the invention of the laser in the early 1960's, LIBS has developed in lock-step with the laser, gaining wider popularity in the early 1980's. Spectrometry or spectrochemistry began in the early 18th century when researchers discovered that different materials emitted different colors of light. Eventually it was determined that each element emitted a unique signature or combination of different wavelengths. This feature became the foundation for chemical analysis using atomic emission.

Prior to 1980, the laser and associated analytical tools were not as sensitive or robust compared to other spectrochemistry techniques like spark or arc-based plasmas and inductively coupled plasma spectroscopy. During this time lasers were occasionally used to ablate samples and introduce vaporized material into an inductively coupled plasma [46], but for the most part LIBS was stalled by the cost and poor performance of lasers and detectors. The first commercial instruments based on laser ablation spectroscopy were introduced between 1964 and 1967 by Zeiss, Jarrel-Ash, and JEOL. These instruments often used a traditional spark across the ablation region and while they could analyze non-conductive samples, they were plagued by inaccuracies and variability [47].

Research in the late 1960's and 1970's included significant work on plasmas generated via laser. Much of this work was published in Russian literature by authors such as Afana'ev, Krokhin, Raizer, Biberman, Norman, and Buravlev [24]. Seminal work by Cremers and Radziemski began in the early 1980's at Los Alamos National Laboratory with time-resolved measurements [51, 53, 23, 22, 21]. At this time the term "'LIBS"' was also coined and its popularity began to grow rapidly.

Detectors

Detection of the plasma emission initially relied on photographic equipment, prisms, and gratings. Unfortunately, this type of detection is unable to remove the continuum emission. The early 1980's also brought widely available photomultiplier tubes (PMT). These devices, along with advancements in pulsed lasers and gated integrators, allowed the ability to synchronize the laser plasma and the amplified detection [62]. Adjusting the gate or delay between the two, it was possible to suppress the continuum emission which occurs at the beginning of the plasma. The next advancement in detection came with the advent of charge-coupled devices (CCD) which use micro-electronic array. This 2-D array can record multiple spectra at the same time, greatly improving the capabilities of LIBS. A combined spectrograph-detector has become the standard LIBS measurement device. The most common modern detector scheme utilizes a Czerny-Turner spectrometer coupled to a intensified CCD (ICCD). High resolution monochrometers are capable of 0.001nm resolution but are

limited to small spectral windows. Different applications have various requirements and a trade-off is made between spectral resolution and spectral range.

1.2 Laser-Induced Plasma Basics

During laser ablation the laser energy is absorbed by the sample material, which is vaporized, atomized and excited. The plasma consists of electrons, ions and neutral atoms. As the plasma expands and cools the optical emission is generated which is characteristic of the sample material. Laser-induced plasma emission is composed of discrete lines of atomic and ionic emission combined with a broadband continuum. The plasma emits radiation as recombination, relaxation of ions, or relaxation of atoms [52].

$$X^+ + e^- \rightarrow X + h\nu \tag{1.1}$$

$$X^{+^*} \rightarrow X + h\nu \tag{1.2}$$

$$X^* \rightarrow X + h\nu \tag{1.3}$$

At early times in the plasma, the emission signal is dominated by the continuum emission. This continuum is generated by electron-ion recombination and free-free interactions (bremsstrahlung). The atomic and ionic emission signals become distinguishable after the strong continuum emission has died down. A schematic of the plasma evolution is shown in Figure 1.2.

The gate width and gate delay shown in Figure 1.2 are instrumentation parameters which can be varied in order to optimize the collection. It is important to open or activate the detector after the continuum has decayed so that it can be filtered out leaving the atomic and ionic signal visible.

1.3 Plasma Morphology

The shape and intensity of an atomic or ionic emission line carries significant information about the plasma conditions and associated element, far beyond identification. The line strength, or emission intensity of a specific emission line depends on the excitation conditions as well as the transition probabilities between the excited and relaxed state. The measurements in LIBS and other emission spectroscopy techniques rely on acquired photon counts that are binned as a function of wavelength. The emission intensity of a specific line or element is sometimes defined differently to reflect experimental and analytical methods. This can be defined as the peak or maximum of the spectral distribution for that wavelength less the background. This can also be stated as the integrated signal above background for the wavelength in question. One method used to reduce error in the measurement is to integrate the area under the signal curve for the entire emission peak. The emission intensity can also be defined as the integrated area of the line fit of the spectral profile.

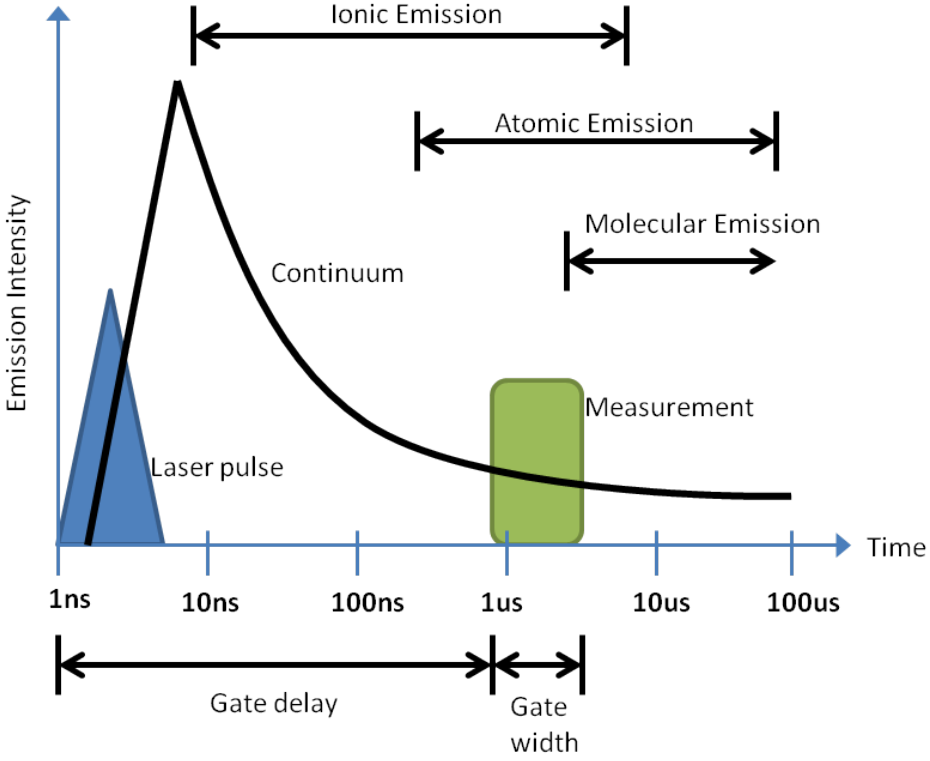

Figure 1.1: Plasma evolution and emission collection timing

Usually a Lorentzian (Cauchy-Lorentz), or Voigt line profile is used. This helps eliminate error introduced by two emission line profiles overlapping . The emission lines are broad due to instrumental resolution, Doppler broadening , and Stark broadening. The broadening or FWHM attributed to Stark effect is the difference between the instrumental FWHM and the Lorentzian curve fit FWHM.

Line Broadening

Determining the shape of spectral emission lines can expose information about the plasma temperature, density and also the absorption and emission coefficients. In the ideal case of a fee atom, the emission takes the form of a Lorentzian profile according to the equation 1.4

$$I(\nu) = \frac{I_0(\gamma/4\pi)^2}{[(\nu - \nu_0)^2 - (\gamma/4\pi)^2]} \tag{1.4}$$

where I_0 is the peak intensity for the line at ν_0, and γ is the radiation damping constant. This profile is the natural profile and occurs for low density plasmas.

Doppler broadening occurs due to random thermal motion and give the line shape a Gaussian profile with a full width half maximum (FWHM) according to Equation 1.5 which tends to dominates near the center of the line shape.[58].

$$\Delta\nu_D = (2\nu_0/c)(RTlog2/M)^{1/2} = 7.16 \times 10^{-7}\nu_0(T/M)^{1/2} \tag{1.5}$$

Dense plasmas common to LIBS have a much more dominant broadening mechanism due to atom interaction with charged particles in an induced electric field. This is referred to as Stark broadening. The electric field in the plasma disrupts the energy levels of ions, thus broadening the line. This line width becomes a useful tool in estimating electron number density, and the FWHM is given by [45]

$$\Delta\lambda_{Stark} = 2w\frac{(n_e)}{10^{16}} + 3.5A\frac{(n_e)}{10^{16}}^{1/4}\left[1 - BN_D^{-1/3}\right]w\frac{(n_e)}{10^{16}} \tag{1.6}$$

where B is a coefficient of 1.2 or 0.75 for ionic and atomic lines respectively, w is the electron impact parameter, and A is the ion broadening parameter, and n_e is the electron number density. This equation becomes extremely useful in order to estimate plasma parameters

1.4 Plasma Parameters

Understanding the laser-induced plasma conditions is of great use both analytically and experimentally. The ability to generate quantitative measurements using LIBS, relies on the ability to determine two key parameters, plasma temperature and electron number density. Many of the plasma measurements require the assumption that the plasma be optically thin. This designation applies when a photon generated by spontaneous emission has a negligible chance of being reabsorbed. This condition occurs for discharge at low pressures with a Maxwell distribution of the electron kinetic energy. In cases where the electron temperature is much higher than the kinetic energy of atoms and ions the assumption is valid. Another assumption that is critical to LIBS plasma analysis is that of local thermodynamic equilibrium (LTE). This condition exists when the magnitude of collision processes in the plasma greatly dominate those of radiative processes. In other words, the probability of relaxation through inelastic collision is much higher than spontaneous emission. In this state there exists a temperature parameter that satisfies the Boltzman, Saha, and Maxwell distributions. The plasma is then able to be described by a electronic excitation temperature and electron number density [63]. Researchers began trying to model plasmas in the early 1990's with various parameters, excitation mechanisms and ablation regimes. It became clear when the assumption of LTE may be applied. It is generally accepted that plasma temperatures less than 11000K at atmospheric pressure with an electron number density greater than $10^{17}/cm^2$ will ensure LTE.

Plasma Temperature

The temperature for a plasma which exists in LTE can be estimated by the relative intensities of separate lines. The plasma temperature represented in terms of relative intensities of two lines from the same element and same ionization stage is given by

$$kT = (E_2 - E_1)/log_e(I_1\lambda_1^3 g_2 f_2 / I_2\lambda_2^3 g_1 f_1) \tag{1.7}$$

where I_1 is the integrated intensity, λ_1 is the wavelength, f_1 is the oscillator strength, E_1 is the excitation energy, and g_1 is the statistical weight. The corresponding parameters with subscript 2 represent the values for the second emission line. It is important to note that these two lines must be of different upper energy levels where $E_1 \neq E_2$. Additionally they accuracy of this method is improved for lines that are very close in wavelength but very far apart in energy levels. This will reduce the spectral error associated with the measurement device and reduce any the effect of slight variation in emission intensity. The error associated with this calculation stems from the intensity measurements and the uncertainty is given by

$$\frac{\Delta T}{T} = \frac{kT}{\Delta E}\frac{\Delta R}{R} \tag{1.8}$$

where $\Delta E = E_1 - E_2$, $R = I_1/I_2$ is the ratio of measured intensities, and ΔR is the uncertainty associated with ratio [45].

Often it is more convenient to use two lines from the different ionization stages. The Saha ionization equation can be combined with the Boltzman excitation equation to yield the following relation

$$ln\left(\frac{I_1^{''} A_2^{'} g_2^{'}}{I_2^{'} A_1^{''} g_1^{''}}\right) = ln\left(\frac{2(2\pi mkT)^{2/3}}{n_e h^3}\right) - \frac{(E_{ion} - \Delta E_{ion} + E_1^{''} - E_2^{'})}{kT} \tag{1.9}$$

This technique is usually less sensitive to measurement noise due to the larger spread in energy levels. Typical pulse energies range from 10-100mJ and result in a plasma temperature of several tens of thousand degrees.

Electron Density

The remaining plasma property necessary for understanding the conditions of the plasma is electron number density. The primary method for calculating this parameter utilizes Equation 1.6. This equation can be simplified for most LIBS experiments where ion broadening is very small to the form

$$\Delta\lambda_{Stark} = 2w\left(\frac{n_e}{10^{16}}\right) \tag{1.10}$$

The values for w, electron impact parameter, have been tabulated by Griem and can be found in [29]. This method of calculation makes no assumptions about LTE. If the experimental conditions are such that the plasma is close to LTE another calculation can be performed,

referred to as the Saha-Boltzman method. Two lines of the same element and different ionization levels can be used in the following equation

$$n_e = \frac{2(2\pi m_e kT)^{2/3}}{h^3} \frac{I_2^{'} A_1 g_1^{''}}{I_1^{''} A_2 g_1^{'}} e^{\frac{E_{ion}+E_1^{''}-E_2^{'}}{kT}} \tag{1.11}$$

Careful attention must be paid when using the calculation and assumptions. There have been many papers upholding the aforementioned calculations, yet additional papers showing errors in the practice and specific exceptions to the rule.

1.5 Laser Ablation

Laser ablation is the use of intense light energy for the removal of material by melting, vaporization, sputtering, sublimation, and ionization. The coupling of laser energy to material removal can occur due to photon-phonon or photon-electron interactions. The parameters governing laser ablation include, wavelength, fluence, pulse duration, beam profile, beam size, frequency, ambient gas type, temperature, pressure, and material type. Due to the interactions of all these parameters it is almost impossible to develop a unified theory to predict the result of a laser ablation event. As these various parameters effect laser ablation, they also effect the laser induced plasma and LIBS signal. The energy density of the laser beam at the focal plane of the objective lens can be calculated using [57]

$$F[r] = \frac{2E_{pulse}k^2}{\pi} \int_0^{a/w_0} \rho e^{-\rho^2} J_0(kr\rho) d\rho \tag{1.12}$$

$$k = \frac{2\pi w_0}{f\lambda} \tag{1.13}$$

where $F[r]$ is the energy density of a modulated Gaussian beam at the focal plane of the objective lens, E_{pulse} is the total pulse energy, k is a characteristic inverse length, J_0 is a zero-order Bessel function, f is the focal length, and a is the radius of aperture. With a Gaussian beam profile, the diameter of the ablation crater can be calculated by [65]

$$D^2 = 2w_0 \ln[\frac{F_{0,peak}}{F_{th}}] \tag{1.14}$$

where w_0 is the beam diameter $F_{0,peak}$ is the peak laser fluence, and F_{th} is the damage threshold fluence.

Nanosecond Ablation

Laser pulses on the order of several nanoseconds provide laser irradiance on the order of $10^6 - 10^{11} W/cm^2$. Thermal processes dominate for laser ablation with irradiance less than $10^8 W/cm^2$ causing the sample to heat, melt, and vaporize. The plasma is formed from

vaporized material being ionized by the incoming laser beam. It is possible to use the heat conduction equation by assuming the problem to be 1-dimensional according to the following [13].

$$\frac{\partial T(x,t)}{\partial t} = \frac{\partial}{\partial x}\left[\left(\frac{\kappa}{C_p \rho_s}\right)\frac{\partial T(x,t)}{\partial x}\right] + \frac{\alpha}{C_p \rho_s} I(x,t) \tag{1.15}$$

where T is the internal sample temperature, x is the distance from the surface, κ is thermal conductivity, C_p is the heat capacity, ρ_s density, and α is the absorption coefficient. Plasma shielding can occur if the plume is near critical density which absorbs part of the incoming beam. It has been determined that an irradiance greater than $0.3 GW/cm^2$ can cause the truncation of the end of the laser pulse [43].

The induced plasmas emission from nanosecond ablation contain strong continuum signal during the laser pulse and continuing several hundred nanoseconds. Ionic emission also dominates in this nanosecond time region while atomic emission occurs after approximately 1 microsecond. Molecular line emission can occur at later times from the recombination of species and interaction with the ambient gas.

Femtosecond Ablation

A femtosecond laser pulse interacts with solid samples in a different way than tradition photothermal ablation. Conducting samples contain free-electrons which can absorb laser energy directly. However in dielectrics, free carriers are generated through multiphoton ionization, avalanche ionization, or tunneling ionization. A single photon from a femtosecond pulse may not have the energy required to promote an electron from the valence band to the conduction band, so multiple photons are required. Additionally, the pulse duration of the femtosecond laser can be shorter than the characteristic time for thermal diffusion and thus the equilibrium equations and assumptions breakdown. When the density of electrons in the conduction band reaches a critical level, ablation occurs [2]. The best indicator of these multi-photon, avalanche, or tunneling ionization mechanisms is the deviation from linear dependence of damage threshold on pulse duration. At pulse durations less than 100 fs, multiphoton ionization is primarily responsible for optical breakdown [39]. The use of femtosecond lasers for LIBS can provide significant benefits due to the high intensity and reduction of thermally related processes. However, more investigation is required in order to understand the plasma physics involved for quantitative and theoretical analysis.

Chapter 2

System Setup

The LIBS system utilized in this study was built with the goals of versatility, repeatability, accuracy, and high throughput. In order to accomplish these goals, a system was needed that would provide accurate and repeatable sample locating abilities, as well as controlling the laser and spectral acquisition. The tool also needed to be user-friendly and intuitive. The final LIBS system consisted of 4 subsystems: sample control, sample/plasma imaging, laser focusing, and laser/spectrometer control.

2.1 Sample Control

Manipulation of the sample is accomplished with three computer controlled Micos stages. The X, Y and Z stages have a range of 120mm, a resolution of 0.2μm and a repeatability of 0.3μm. These stages are controlled with the Corvus Eco motion controller which communicates with the PC via USB connection. The native communication software provided with the system is Winpos. This communication terminal allows discrete commands to be sent to the motors. It is also possible to write a script for the motors to carry out in the native language. Micos also provides a LabView driver which was incorporated in to the custom LIBS software. This software allows for discrete movement of each stage with variable step sizes as well as command line macros to send a motion routine. The stages provide no absolute position feedback to the computer so they must first be initialized when the software system is engaged. However, the stage velocity and acceleration parameters are stored in memory the motion controller. This subsystem allows precise control of the sample and greatly improved the throughput of measurements.

2.2 Sample and Plasma Imaging

The imaging system consists of a Navitar motorized 10X zoom lens, coaxial fiberoptic illumination, computer controlled programmable light source, ThorLabs CCD camera, and 3x,5x, or 10x microscope objectives. The motorized zoom lens is controlled via usb or RS-

232 communication through a separate motor driver and power supply. The proprietary software included with the unit was used to adjust the zoom, but was not included in the custom LIBS software. The CCD imaging camera is controlled and powered through USB connection to the PC. The imaging software used was uEye Demo included with the camera and was not incorporated into the custom LIBS software. The laser and sample imaging system utilize the same microscope objectives. The plasma imaging system consists of a 25.4mm quartz focusing lens, which images the plasma onto a fiberoptic bundle. An alignment system was created to allow for fine independent adjustments to the focusing lens and fiberoptic cable. This configuration allows for various fiberoptic cables to be used ensuring proper alignment.

2.3 Autofocusing

One of the main advantages of the LIBS system is the autofocusing sub-system. Samples can be adjusted to the same position and focusing conditions and there is much better repeatability shot-to-shot. This system consists of a Micro Epsilon laser range sensor which uses a class III laser directed at the sample and a sensor measuring the scattered or reflected light. The company provides a LabVIEW driver allowing the system to be included in the LIBS control software. The custom software includes a auto-focusing sub-routine allowing the user to set a desired range and tolerance. The elevation stage then adjusts in order to bring the sample to the desired position. The sensor laser diode can be turned on and off along with the auto-focusing routine, so as not to interfere with any spectral collection. One of the disadvantages is that the system must be oriented at an angle to the sample. Ultra smooth samples cannot be measured with the range finder because it requires scattered light.

2.4 Laser and Spectrometer Control

An independent 8-channel delay generator (Berkely Nucleonics Corporation) controlled via LabView allows the system to operate using almost any combination of laser and spectrometer. This device allows the independent triggering and syncing of up to 8 outputs. This was used to control the timing between laser flash-lamp and Q-switch as well as the timing between the laser, shutter and spectrometer. Different configurations of laser and spectrometer require slightly different triggering routines to produce the same output. This system controls the laser power of Nd:YAG lasers by varying the delay between the laser flash lamp and Q-switch.

Nanosecond LIBS with Avantes Spectrometer

This configuration requires the user pay special attention to the timing of signal pulses. The Avantes spectrometer is very limited with regard to timing, and temporal resolution. The spectrometer has a minimum gate width of 1.05ms, and a minimum internal gate delay of

3.028μs. However, the time it takes for the laser to arrive at the LIBS system is shorter. Therefor the spectrometer must be triggered prior to the Q-switch of the Nd:YAG laser in order to sample the emission at optimal conditions. Adjusting the emission acquisition can be accomplished by moving the collection optics laterally with respect to the plasma, or adjusting the angle of observation. It should be noted that the base and core of the plasma presents more background emission than the top or sides.

Nanosecond LIBS with Princeton ICCD

Using an Nd:YAG laser with a Princeton ICCD is easily accomplished by triggering the laser and the camera at the same time, regardless of the specific monochrometer being used. The spectrometer control software, Winspec, provides the ability to adjust the acquisition duration and delay. The minimum internal gate delay for the ICCD is less than 1 ns, and the minimum gate width is 2.2 ns. With this configuration the entire ablation event and subsequent plasma emission is accessible. This simplifies the triggering and timing by allowing the laser's Trigger-Out signal to trigger the spectrometer, thus removing the need for a delay generator. However, the LIBS system utilizes a delay generator and the spectrometer trigger signal is synced to the laser Q-switch signal.

Aligning the collection optics is a very important aspect to optimal LIBS spectral acquisition and sensitivity. It is generally assumed that the plasma is small relative to the imaging field, and the focused image on the fiber. The collection optics and fiber should be installed in approximately the correct location and alignment relative to the optical focal length. A low-power Class III or lower He-Ne laser should be used to aid in alignment and can be coupled through the end of the fiber opposite the direction of emission collection. In this configuration the alignment laser will be focused onto the sample so that the angle, position and lens location can be further refined. Now the ablation laser can be used to aid in alignment. In a relatively dark environment the laser is operated at 1-10Hz and the plasma is focused onto the fiberoptic cable. A narrow piece of paper or alignment aid can then be inserted between the optical collection lens and the fiber so that the user can confirm that the plasma image is being focused correctly onto the fiber. The termination of the fiber can then be installed appropriately into the spectrometer. At this point the plasma emission should be observed through the spectrometer software. If nothing is is observed the timing and triggering commands should be checked. Final adjustments to the optical collection optics can be made using the spectrometer signal to optimize peak intensity and minimize background. The Navitar motorized zoom lens and CCD imaging camera should be aligned by zooming in as far as possible and adjusting the height of the elevation stage to bring the image in focus. Next the system is zoomed out all the way and internal lens is adjusted manually to bring the image in focus. Repeating these steps a few times will ensure the image stays in focus throughout the range of magnification. The image position, rotation, and alignment are modified using the 3 adjustment screws on the CCD adapter collar. The camera can be rotated and centered using these screws. Alignment can be confirmed by

choosing an object in the center of the image and increasing the magnification to ensure that the object stays in the center.

Chapter 3

Ultrafast LIBS of thin film doped oxides

3.1 Introduction

Ultrafast lasers have gained popularity over the past decade, and are becoming smaller and less expensive. It was previously summarized that femtosecond LIBS provides no analytical benefit over traditional LIBS, other than the laser ablation characteristics [58, 45]. However, short laser pulses have significant advantages for micromachining of bulk materials and the unique processing of dielectrics [41, 69, 49, 9, 10, 68]. Thin films pose additional unique challenges due to their dimensional constraints, morphology, and optical properties. In order to selectively ablate thin films with nanosecond or longer pulses, careful attention must be paid to the laser fluence as well as the optical properties of the material layers and ablation thresholds. Due to the nature of traditional photothermal ablation in ambient conditions there is usually a large heat affected zone from thermal confinement and excessive molten or redeposited material on the surface. Ultrafast laser pulses are shorter than the thermal diffusion time scales and can induce ablation with a relatively small thermally modified region [31]. These short pulses provide enhanced control for scribing thin films, and laser induced forward transfer [48, 64, 37]. Ultrafast ablation also produces high-density plasmas. These advantages apply to the LIBS analysis of thin films and provide the ability to finely control the ablation depth and prevent substrate interference. In a laboratory environment the substrate material is often known and it is easy to subtract that out from the collected data. In the field, selectively ablating the film of interest significantly reduces the need for post processing of the data. Thin films on painted surfaces pose unique challenges to LIBS. Nearly every post-World War I painted surface contains an emulsion of TiO_2 as its base to which other pigments are added. This makes the analysis of residues or films on painted surfaces difficult. TiO_2 is also added to sunscreens, lotions, and toothpaste. TiO_2 films are also used extensively in dye-sensitized solar cells for their porosity and high surface area [59]. This transition metal oxide produces a very broad and noisy signal which makes

compositional analysis using plasma spectroscopy very difficult. This material system was chosen for its complexity and wide use to investigate the advantages of ultrafast laser pulses for thin film LIBS, and the analytical issues associated with TiO_2.

3.2 Experimental Setup

This set of experiments was conducted prior to construction of the system described previously, and the specific experimental setup begins with the output from a Ti:Sapphire (Mai-Tai oscillator coupled to a TSA-25 amplifier, Spectra-Physics) femtosecond laser delivering 100fs pulses at 10Hz. The fundamental beam (800nm) and frequency tripled beam (266nm) are passed through a series of mirrors to the ablation chamber. An additional Q-switched Nd:YAG laser operated at 266nm with a pulse width of 4ns was used for comparison. The selected beam was focused through a long focal length quartz plano-convex lens (f = 63mm) normal to the sample surface on an XYZ motorized stage (Thorlabs RB13S) for positioning and scanning. A fiber optic cable was positioned at 45 degrees extremely close to the ablation region to collect as much light as possible. The collected emission is passed through the fiber optic bundle and an adjustable slit to a Czerny-Turner spectrometer (SpectraPro-2150i, Acton Research Corporation). Two switchable gratings were used at 150 and 600grooves/mm (500nm blaze and 300nm blaze, respectively). The spectra were collected and measured using an ICCD camera (PI-MAX, Princeton Instruments). A mechanical shutter was synchronized with the laser output and used to trigger the spectrometer. This allows one to select single laser pulses at the desired frequency, and to vary the gate width and delay. The wavelength calibration of the spectrometer was carried out using an Hg line-source calibration lamp (Newport 6035).

Thin films were prepared using aerosolized TiO_2 powder (Aeroxide P25, Nippon Aerosols) with an average size of 21nm. The MgO dopant was added in the form of high purity chemical grade 22-mesh powder (Puratronic). The powders were combined gravimetrically, then milled and combined with a solvent of 10% acetic acid in distilled H_2O. Smestad and Gratzel describe this procedure in detail for the production of semiconducting layers for dye-sensitized solar cells [59]. A mortar and pestle is used to produce the base solution. The powder is added and then $1mL$ of acetic acid solution is added and the mixture is ground into a uniform paste. This process of adding $1mL$ of dilluent and grinding the mixture for 1 minute is repeated multiple times until the final concentration and consistency is achieved. This mixture serves as a master solution. Further dillutions were prepared in order to vary the viscosity. The solutions were the blade-cast or spin coated at 6000 rpm for 60 seconds on ultra-pure quartz substrates. Different dilutions were used to produce different thickness. The films were then allowed to slowly air dry at 25C in a controlled environment to prevent any cracking or contamination. In order to remove and organic solvents or remaining moisture, the samples were annealed at 500C for 4 hours with a 2 hour ramped heating and 2 hour cooling period.

The prepared films were then analyzed using a white light interferometer to measure

Table 3.1: Thickness measurements of TiO_2 thin films.

Dilution	Coatings	Thickness (nm)	Film RMS (nm)	Substrate RMS (nm)
1:2	1	4.55	4.16	0.48
1:2	2	5.17	3.01	0.52
1:2	5	14.30	2.37	0.64
1:2	10	22.36	4.62	0.66
1:3	1	0.43	2.80	0.53
1:3	2	0.60	3.75	0.52
1:3	5	5.11	7.59	0.67
1:4	5	1.89	3.01	0.49
1:5	5	1.79	1.55	0.70

the thickness. This data was collected and averaged for multiple film preparations over multiple measurement locations. A small group of samples were measured during the process development and their thickness data is shown in Table 3.1 as an example. The transmissivity of these films can be seen in Figure 3.1 this information can be used to aid in determining the thickness of the subsequent films. It is also important to understand the optical properties of the films as many of the ablation parameters depend on the laser material interaction. The thickness measurements and optical properties of these samples produced during process development were conducted using glass microscope slides, while the ablation and LIBS measurements were made using quartz substrates. A subset of samples were prepared on both substrates and there was no appreciable difference between the thickness measurements. The optical properties only differed by the amount contributed from the substrate at UV wavelengths. High purity quartz substrates were chosen for the ablation experiments due to the better adhesion of the films which did not exfoliate or crack like those prepared on glass.

3.3 Results and Discussion

In this study the LIBS data was taken from a new spot on the sample each time. While ultrafast laser pulses are effective in selectively ablating a large quantity of the oxide film, substrate emission can be seen if multiple shots are used. Several films were prepared of different thicknesses ranging from 0.15-15.0μm. The fundamental (800nm) femtosecond and 3rd harmonic (266nm) output beams were used in the same LIBS setup with the same focusing objective. The beam spot was approximately 80μm in diameter. Both sets of experiments using the femtosecond laser produced very clean craters, removing the film while leaving the substrate relatively undisturbed. The ablation craters were measured with a scanning white-light interferometer (NewView 6K, ZYGO). Representative depth profiles of the ablation craters for various thickness films are shown in Figure 2 for the 266nm ultrafast laser at 1.5 J/cm^2. The nanosecond 266nm beam produced damage of the substrate and Si

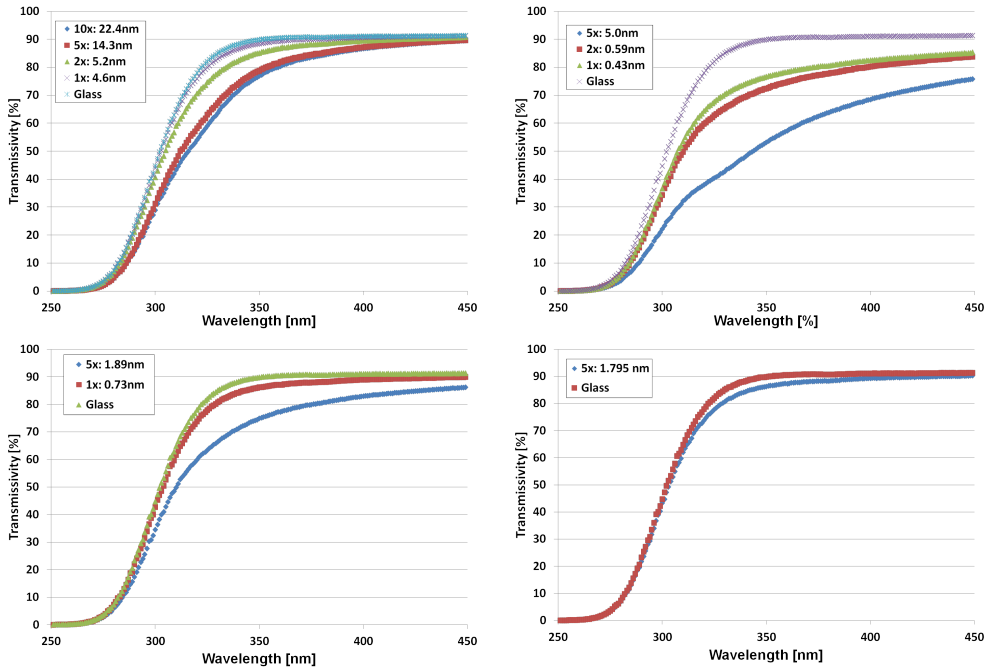

Figure 3.1: Optical properties of TiO_2 thin films prepared at 1:2, 1:3, 1:4 and 1:5 dilution

peaks were seen in ablation of films less than 100nm thick.

Samples prepared by blade-casting and spin coating were made with varying heavy metal dopant levels. The samples were analyzed with the ultrafast LIBS system and the data collected with 5ns sequential gating for different wavelength ranges. The strongest Mg peaks were used to analyze the composition. Specifically the $Mg - II$ 279.55 - 280.27nm line associated with the $2p^6 3s - 2p^6 3p$ transition was used. The best detection was obtained by using the signal acquired during the first 5ns of detectable atomic emission. After this time the dopant signal decreases more rapidly than the matrix material and the relative intensity is diminished. The plasma intensity also decreases with laser energy as seen in Figure 3.2.

The collected spectra from the sequentially gated ICCD was processed and normalized. The integrated peak ratio technique for Mg/Ti for $Mg - II$ 279.55-280.27nm and $Ti - I$ 375.286nm was used as a qualitative comparison and analyzed for the various dopant concentrations and lasers used. The data presented in Figure 3.3 represents an acquisition with the gate delay set just after the broad continuum emission 15-27ns after the laser pulse and a gate width of 5ns. Ultrafast laser pulses at 800nm provided the best detection of Mg dopant concentrations in a $TiO_2 + MgO$ background down to 0.006 weight percent. However, due to the noisy background TiO_2 signals, the statistical limit of detection value is higher. Using the standard 3-International Union of Pure and Applied Chemistry (IUPAC) definition, the limit of detection for this experimental setup and material system was 0.301, 0.826, and 1.194 weight percent for femtosecond 800nm, 266nm, and nanosecond 266nm

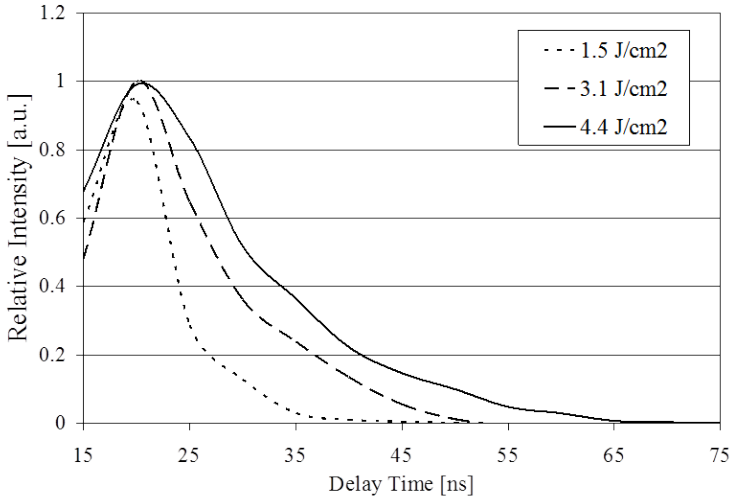

Figure 3.2: Relative intensity of $Mg-II$ LIBS signal as a function of delay time and fluence

respectively. The coefficient of determination, or R^2 value, for the linear regression analysis used was 0.9506, 0.9958, and 0.9702 respectively.

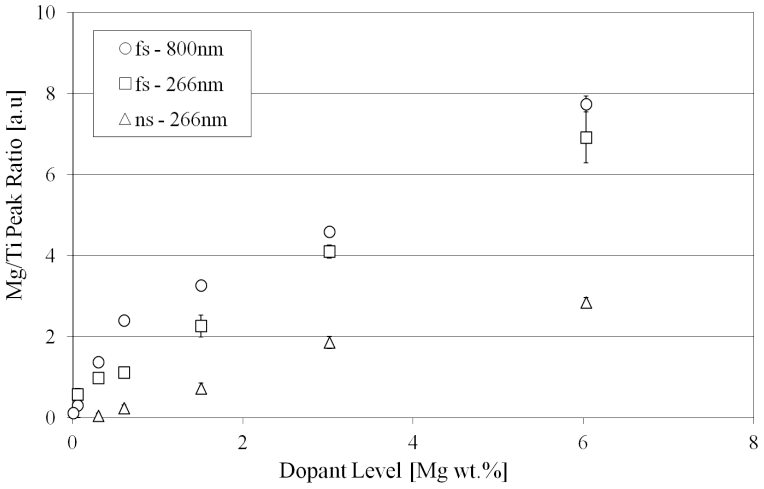

Figure 3.3: Intensity ratio of $Mg-II/TiO_2-I$ LIBS signal as a function of Mg concentration

The ablation on quartz substrates produce very clean craters which remove most of the film, leaving the underlying substrate relatively undamaged. A 3D map of their surface is shown in The cross section of ablation craters showing the profile are shown in Figure 3.6.

A scanning electron micrograph of the ablated film is also shown in Figure 3.4. The ability to generate these types of craters for thin film analysis is highly desirable. Limiting the contribution from the substrate allows the best chance for accurate film measurements.

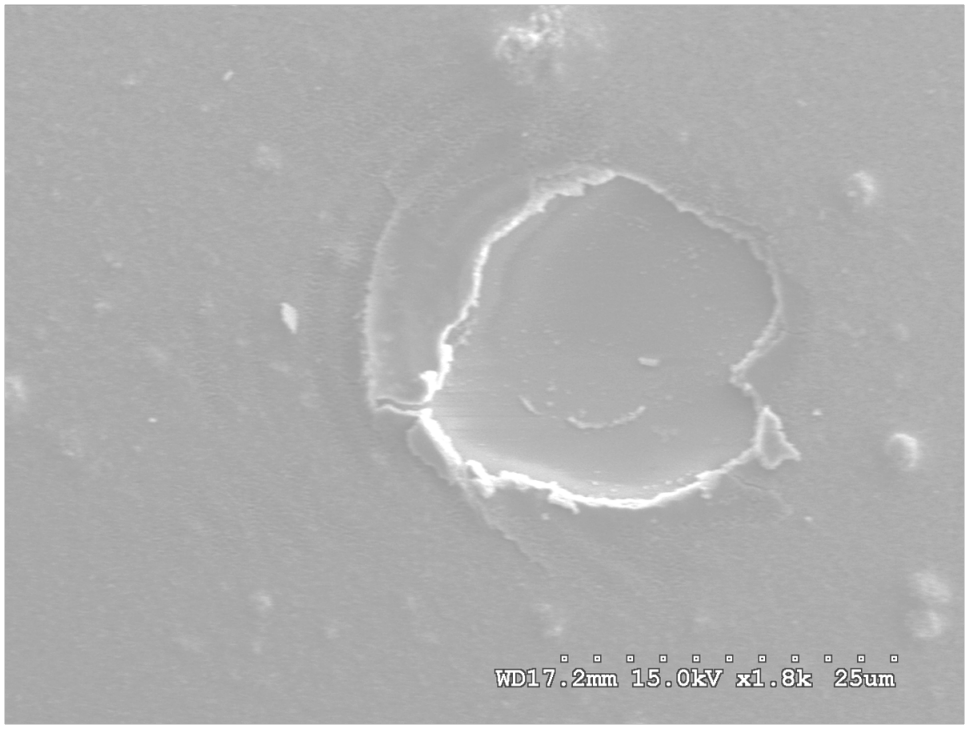

Figure 3.4: SEM image of ablation crater for 700nm thick TiO_2 film

3.4 Conclusions

The use of femtosecond lasers for LIBS provides many significant benefits over traditional techniques for thin film analysis. Single-shot ablation provides excellent material removal and excitation without substrate damage or interference over a wide range of film thicknesses. The benefit of selective ablation and better control of material removal may overcome the additional expense of ultrafast lasers for thin material analysis and modification. This LIBS configuration successfully detected Mg dopant in a film of TiO_2 down to 60 ppm.

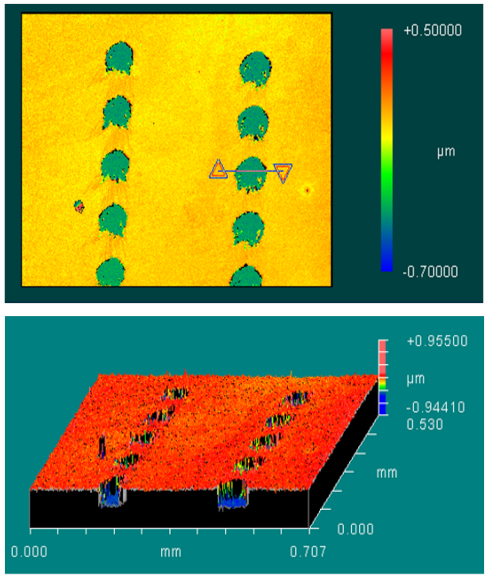

Figure 3.5: Interferometric 3D surface map of TiO_2 ablation craters

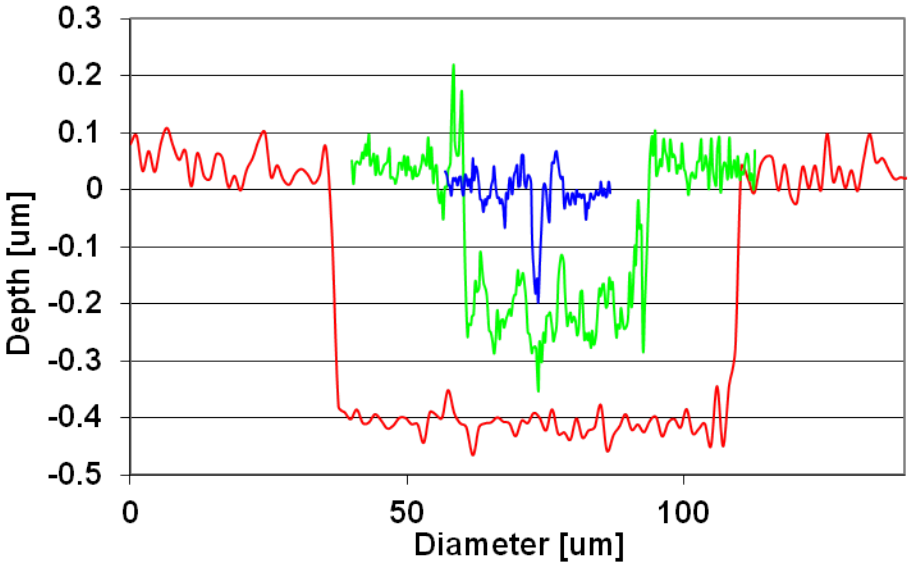

Figure 3.6: Ablation crater profile cross-section for 266nm wavelength femtosecond ablation of 400nm, 250nm, and 150nm thick TiO_2 films

Chapter 4

LIBS of Organic Thin Films

4.1 Introduction

Laser ablation of thin films is a relatively new and exciting researching area. This technology is used in a wide variety of industries with a multitude of material systems with different functionality. Specifically, the ablation of thin transparent organic films presents unique challenges and opportunities for laser ablation based material modification and analysis. These materials exist as protecting coating , surface modifiers to improve performance, and as encapsulating films [60]. They can also act as functional layers or materials themselves [36, 25].

This research investigates a new way to study these complex materials and various permutations of them. The use of laser ablation as a means of analysis for this type of material system has been rarely studied due to the complexity in ablation process. An important factor in laser ablation is the material ablation threshold which can change with the laser spot size [34], which can alter the analytical results. In addition, other variables can effect the laser ablation such as wavelength, pulse duration, polarization, pressure, temperature, gas type, beam profile etc. While many of the variables were held constant, This study strives to probe some of the phenomena relating to thin film ablation which alter the plume dynamics [32, 50, 20, 8]. Materials of different nature in contact with one another form an interface, which might have special properties relating to the ablation of one or both of the materials in contact [27]. Optical properties are also important in laser-matter interaction and the different optical paths and absorption coefficients of materials can dramatically affect the ablation process, plasma formation and the emission of the species. Regarding the analytical analysis of trace materials [44] or solid residues over a substrate surface, valuable information can be obtained by the ablation of the material system. This may include improved analysis of the substrate assisted by the thin film or the improved ablation/spallation process of the films assisted by the substrate. The processes involved depend on the optical properties of the materials to be ablated, but once the ablation is taking place the behavior of the plasma and ablated species depends on the mechanical properties of the substrate and thin film. These

properties change with film thickness and laser fluence [55]. Finally, the laser absorption by substrate and film independently has a role in ablation process. In a weakly absorbing film the laser absorption by the substrate is more important and becomes the dominant agent of the ablation. The interaction between substrate and film is further confounded when weakly absorbing films have different thicknesses. Although the phenomena can be complicated it provides information about the mechanisms involved and the energy transfer during the process, which has consequences in optical emission and can be used to enhance the analytical capabilities of laser ablation based techniques.

Further studies in this field have the potential to open new applications. Possible implementations of this work in the field of material science might solve some of the previous limitations. In pulsed laser deposition (PLD) of organic polymers it is very difficult to maintain the stoichiometry of the original polymer, so the spallation of the organic films assisted by substrate ablation can yield an improved ablation product [26]. Also, the plasma confinement induced by the film can be used to overcome matrix or elemental fractionation effects.

The optical properties of the materials dictate two primary ablation regimes. Either the laser energy is absorbed by the films or by the substrate. In the first situation the ablation is governed by the film and plasma formation and is not dependent on the substrate properties. The resulting information obtained by the plasma is mainly due to the films. In the second situation the ablation is governed by the substrate absorption and the information provided by the plasma is due to both the film and substrate materials [33]. In this sense the film thickness influence in ablation and emission seems to be valuable in order to study the system. Spallation process is observed in the films [67] and modifications in plasma plume are studied. Some ICCD images are used to show the main shape and size differences in the plume. The mechanisms involved in the spallation process as well as the plasma time evolution are studied. The changes in the plume are attributed to different pressures in the plasma expansion. So, a calculation of the pressures has been done to evaluate the energy released followed by a fast plume expansion.

4.2 Experiment

The instrumental set-up used includes a set of lasers, Minilase II and Tempest 10 (1064 nm and pulse duration 4 ns) and EKSPLA, model NL 303D/SH; (1064 nm, 10 Hz, pulse duration 4 ns). Also a high resolution spectrometer, Spex 1250 M (1-m focal length; 1200-grooves/mm grating) coupled to an ICCD camera. The resolution power of such spectrometer is 0.006 nm. For the study of the craters left by the laser an optical profilometer, NewView^{TM} 6000 Series (3D Optical Surface Profilers), has been used.

4.3 Samples and samples preparation

The sample used as substrate was a polished single crystal silicon $< 111 >$, which presents a very flat surface, ideal for the kind of studies carried out. The material used as an organic film is a commercial nail strengthener. The ingredients are: Ethyl Acetate, Butyl Acetate, SD Alcohol 40B, Nitrocellulose, Adipic Acid, Neopentyl Glycol, Trimellitic Anhydride Copolymer, Isopropyl Alcohol, Triphenyl Phosphate, Trimethyl Pentanyl Diisobutyrate, Camellia Sinensis Leaf Extract (Green Tea), Etocrylene, Benzophenone-1, Dimethicone, Butylene Glycol, Violet 2 (CI 60725). This organic film material was chosen for its excellent adhesive properties, ease of application, optical transparency and hardness.

Ethanol based dilutions of the organic solution were made at different concentrations to obtain variations in film thickness during the spin coating process. Solutions of $MgCl_2$ in Ethanol were made to be added to the nail strengthener solutions in order to have a tracer element (Mg) in the films. $MgCl_2$ is miscible in ethanol as well as the most of the ingredients of nail strengthener.

4.4 Results and discussion

Optical Properties

Laser ablation of thin films is strongly dependent on the absorption of laser energy by the films. There are two extreme situations in which radiation is strongly or weakly absorbed by the films. In the case of strongly absorbing films, the ablation takes place at the film surface. In the case of weakly absorbing films on an absorbing substrate, the ablation primarily takes place at the interface. The specific ablation regime depends on the optical properties of the material, film thickness, laser wavelength and intensity.

In the work of Bose et al. [14] a confinement of heat within a depth is defined for weakly absorbing materials, which is determined by the absorption coefficient α. In strongly absorbing materials $1/\alpha << L_p$, while in weakly absorbing materials $1/\alpha >> L_p$, where L_p is the thermal diffusion distance. Then, the energy absorbed has been defined as:

$$Q = I_0(t)(1 - R)e^{(-\alpha x)} \tag{4.1}$$

where, R is the reflectivity, α the absorption coefficient and $I_0(t)$ the intensity of laser beam.

Table 4.1 shows the absorbance, transmittance and reflectance data that these films present at the laser wavelength used. This table insures that the optical properties of the films are not changing significantly with thickness and can be considered weakly absorbing in the range being studied.

During the ablation of transparent organic films on highly absorbing substrates the plasma is produced near the interface and can erupt through the film causing significant

Table 4.1: Optical properties of the organic thin films.

Thickness (μm)	Transmittance (%) @1032 nm — @1064 nm	Reflectance (%) @1032 nm — @1064 nm	Absorbance (%) @1032 nm — @1064 nm
0.365	99.246 — 99.263	0.485 — 0.476	0.268 — 0.260
0.458	99.639 — 99.631	0.307 — 0.298	0.053 — 0.070
0.863	99.400 — 99.422	-0.078 — -0.081	0.680 — 0.656
1.280	99.327 — 99.319	-0.526 — -0.474	1.198 — 1.156
1.624	99.420 — 99.362	0.506 — 0.462	0.175 — 0.073
2.430	98.872 — 98.890	-0.906 — -0.774	2.034 — 1.883

damage and spallation. In such a process, the amount of mass from the film contributing to the plasma is difficult to evaluate.

Influence of the Film Thickness: Time Resolved Imaging

One of the most informative ways to measure the influence of film thickness on ablation is to investigate the resulting plasma emission. In this study, the composition of the substrate was known (Si) and magnesium was added to the film as a tracer element. As a result, the plasma emission can serve as a way to investigate the ablation efficiency and plasma parameters as a function of film thickness.

Fig. 4.1 (A) and (B) show the emission intensities of silicon and magnesium atomic lines (Si I 288.15 nm and Mg I 285.12 nm) as a function of shot number and film thickness for nanosecond ablation as a function of shot number and for a single shot respectively. Silicon emission comes from (100) n-Type single crystalline substrate. Magnesium emission comes from a trace amount of 1 % molar concentration, which was added to the organic thin films.

Fig. 4.1 (A) shows the trend of intensities obtained in nanosecond ablation, illustrating how the first pulse of the series become weaker for silicon at greater film thickness. Also, thicker films produce a plasma confinement, which presents a larger restriction to the expansion and emission of the plasma. The trend in the data series exhibited by silicon and magnesium signal is different, as expected. Silicon intensities remain almost constant within the data series, suffering a slight decrease due to a change in focal conditions. Magnesium intensities suddenly decrease after the first shot because once the ablation-spallation of the film is complete, there is no film and consequently no Mg available in the plasma to participate in the optical emission.

In Fig. 4.1 (B) the information provided by the graph suggest that increasing film thickness does not increase the amount of film material in the plasma. Silicon emission signal is also affected by the thickness and the intensities observed were lower at larger film thickness. In this case, the film is inhibiting the silicon ablation. The decreasing intensities observed for silicon with film thickness suggest a lower presence of silicon in the plasma. Magnesium intensities are very consistent in the range of thickness, which suggest that the

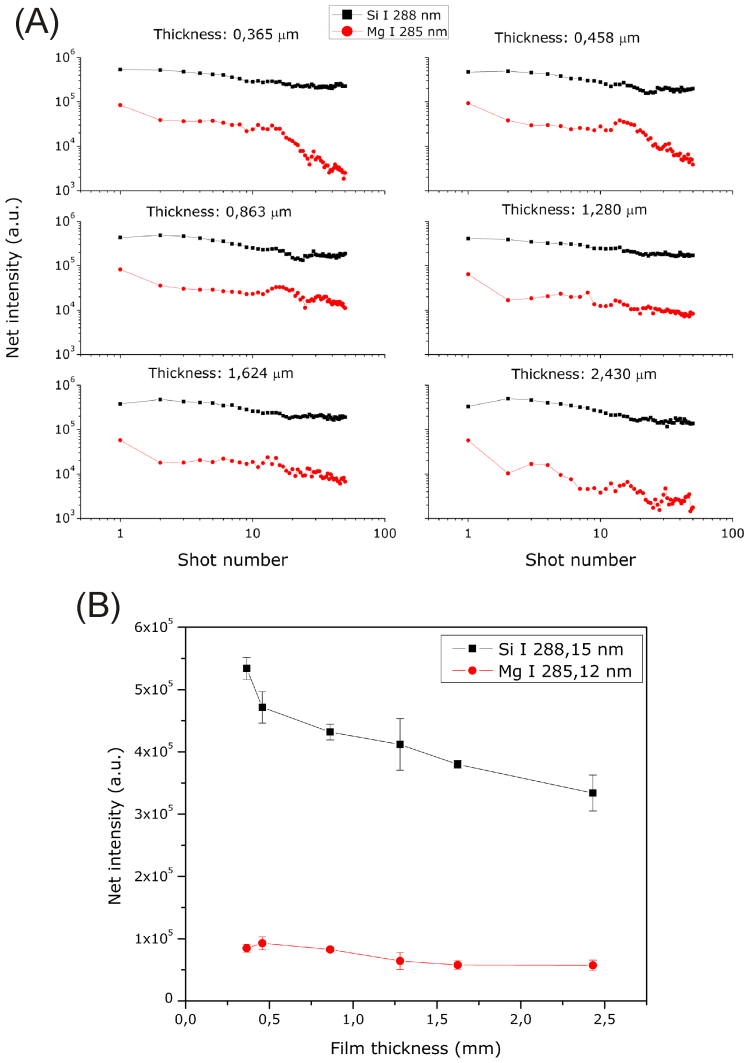

Figure 4.1: Net intensities of Si-I 288.16nm and Mg-I 285.21nm for nanosecond ablation (A) 50 shots and (B) single shot.

amount of material from the films in plasma remains roughly constant with an increased film thickness.

Complementary to the information provided by the emission intensities, a study of the craters also provides information about redeposition of the ablated material and the surrounding affected area. These features are not often studied but are very important to obtain reliable results, specifically in thin film ablation where there is significant redeposition due to the physical properties of the plasma and organic film.

Fig. 4.2 shows the craters formed on the samples for femtosecond and nanosecond laser ablation for the range of film thickness studied.

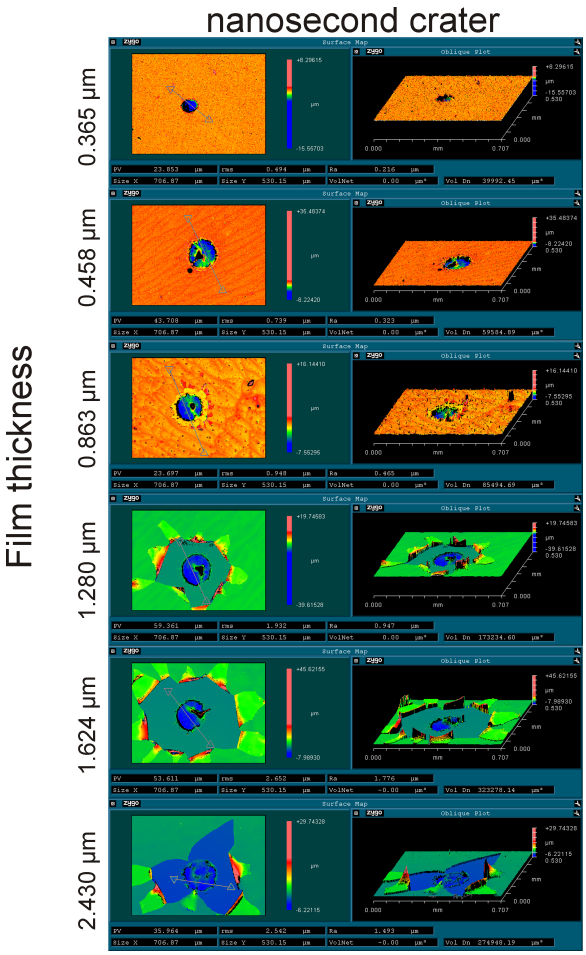

Figure 4.2: White light interferometric mapping of femtosecond and nanosecond ablation craters as function of film thickness

Pictures of the craters, femtosecond as well as nanosecond craters, can be classified into two groups, the thiner films (0.36-0.86 μm) on which the affected area is just the area of the crater and the thicker films (1.28-2.43 μm) on which the affected area is a large area surrounding the craters.

In this figure the splashing of films at a thickness of 1.28 μm for nanosecond ablation can be observed. This phenomenon is not observed for femtosecond ablation on which a larger thermally affected area is shown in films thickness over 1.28 μm.

Previously mentioned for transparent films, the response of the substrate (silicon) to laser radiation is the main contribution to the plasma formation. The energy transfer between the substrate and the film is crucial in the ablation process and also the accumulation of energy underneath the films may produce an enhancement of the ablation rate. The plasma formed on the substrate can push through the film, producing differences in the substrate ablation and plasma morphology. In this process the ablation of the thin films is assisted by

the plasma formation on substrate.

In Fig. 4.3 crater volume and ablated mass for nanosecond ablation are shown. Mass removal in the nanosecond ablation tends to be larger at increased film thickness. The main change in mass removal during ns-ablation takes place between 0.365 nm and 0.458 nm film thickness. Results observed in this section suggest a variation of plasma parameters with film thickness.

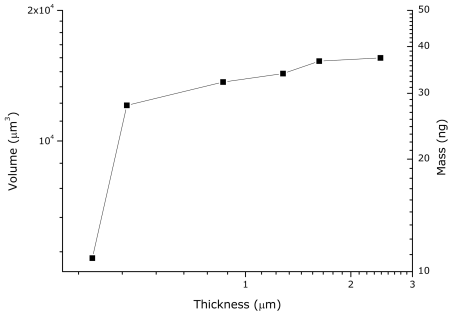

Figure 4.3: Crater volume and ablated mass for femtosecond and nanosecond laser ablation as a function of film thickness

Plasma parameters

Fig. 4.4 (A) shows atomic emission of Si I 288.16 nm and ionic emission of Mg II 280.27 nm, as a function of film thickness.

In Fig. 4.4 (A) atomic Si emission as well as ionic Mg emission have a similar behavior until 1.28 μm film thickness, in which atomic emission tends to rise and ionic emission tends to decrease, giving information about the degree of ionization in the plasma. This is probably a combined effect due to the amount of material and temperature in plasma plume.

In Fig. 4.4 (B), the plasma parameters [30] of temperature and electron number density can both be observed to decrease with the film thickness.

The ablated mass remains approximately constant with film thickness, except for thinner film (0.365 μm). The temperature decreases with film thickness and the amount of energy per unit mass is lower with increasing film thickness. Therein, the plasma must be less ionized at larger film thickness. This can be clearly seen with the decreasing intensity of ionic species.

The combined effect between amount of mass and temperature in the plume indicates that the ablated mass has a principal role in the ablation of silicon and spallation of the films. The main consequence that the total amount of material in plasma has is the energetic distribution of the ablated material inside the plasma, which directly affects the species emission. In other words, a greater amount of material in the plasma produces a greater dissipation of the energy which produces plasma with a lower energetic state. So, plasmas

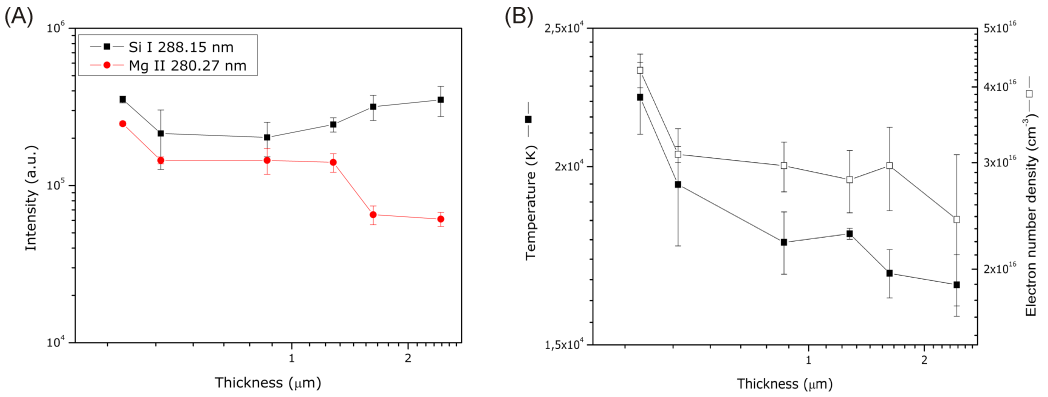

Figure 4.4: (A) Atomic emission of Si-I 288.16nm and ionic emission of Mg-II 280.27nm, as a function of film thickness. (B) Plasma temperature and electron number density, as a function of film thickness

with lower temperatures are generally less ionized. If the ionization degree of the plasma is low, the ionic emission lines should be less intense due to the number of emitting species.

Laser fluence impact on thin film spallation

In this spallation process, the thin films suffer damage due to the shockwave and plasma formed beneath them on the silicon surface. The shockwave and high plasma temperatures are the main reasons for spallation of these thin films.

Different degrees of spallation can be described. These mechanisms depend on the film thickness and laser fluence. Figure 4.5 shows the three different mechanisms proposed as a function of laser fluence for the same film thickness.

To investigate effects of laser energy on ablation of these thin films, a study of the craters as a function of the laser fluence is done for nanosecond laser ablation. A set of electron micrographs were obtained to observe in detail the traces left by the laser. The non-conductive organic thin films were coated with gold, approximately 2nm in thickness, after ablation prior to imaging. The study of these craters provides an important source of information about the processes taking place during the ablation. In Figure 4.5 SEM pictures of 1.280 μm thickness film are observed for different fluence levels.

The pictures suggest three possible outcomes as a function of laser fluence. For the lowest fluence investigated, when the substrate is coated with a thin film and exposed to the same fluence, the silicon surface is damaged. In this case, the picture suggest that plasma opacity at early times (during laser pulse duration) [12, 40, 54], produces the ablation of the film in the laser spot area.

At intermediate fluence level (11.6 Jcm^{-2}; I = 2.90 $GWcm^{-2}$), the amount of energy accumulated at the silicon-film interface induces stress in the films, Fig. 4.5 (B), but is not enough to produce the self-peeling of the films. So, the process might be more dependent on

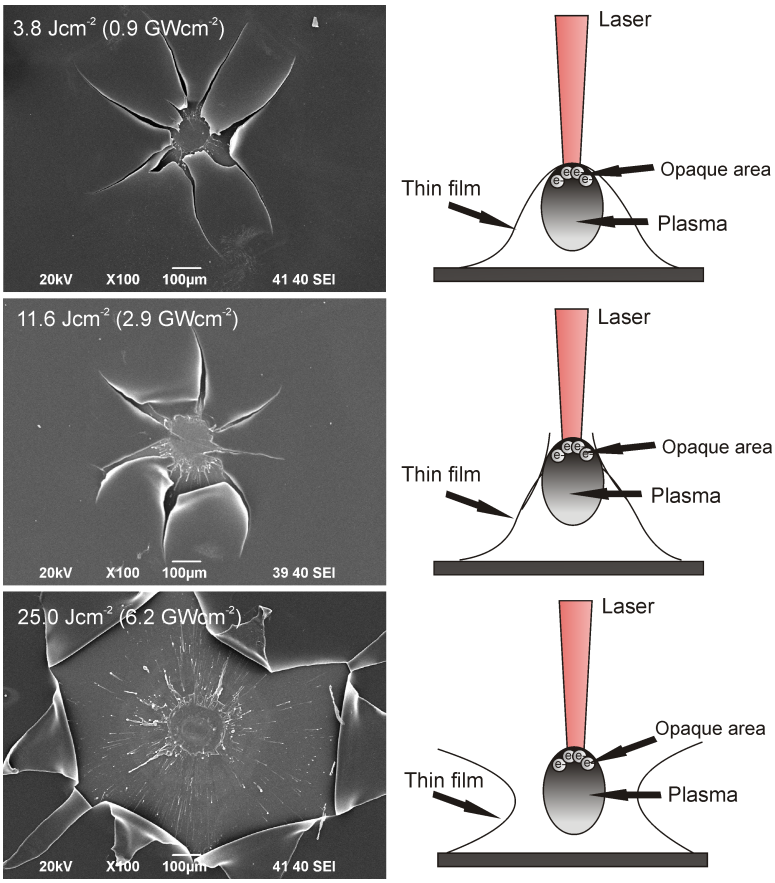

Figure 4.5: SEM images of nanosecond craters for a 1.280 μm thick film deposited on single-crystalline silicon (111) (A) at fluences of: F = 3.8 Jcm^{-2}; F = 11.6 Jcm^{-2}; F = 25.0 Jcm^{-2}. Picture of a folding back of the film due to the plume expansion at F = 25.0 Jcm^{-2} are shown.

laser fluence than on laser irradiance. In fact, self-peeling of the films does not take place in femtosecond ablation mainly due to the lower fluence level and shorter plasma lifetime.

Imaging experiment

Time resolved imaging experiments have been done for silicon and silicon with thin films deposited. This experiment allows us to better understand the changes in plasma emission of silicon due to a deposited thin films. Fig. 4.6 shows the ICCD images obtained for the whole range of film thickness under study at different delay times.

Pictures of the plasma emission for bare silicon and silicon with the organic thin films are shown in Fig. 4.6. The differences in shape and size, between the two types of samples can be easily seen in the figure. At short delay times (0-50 ns) the plasma intensity of bare silicon is more intense than the thinest films (0.36-0.86 μm) but less intense than the thickest films.

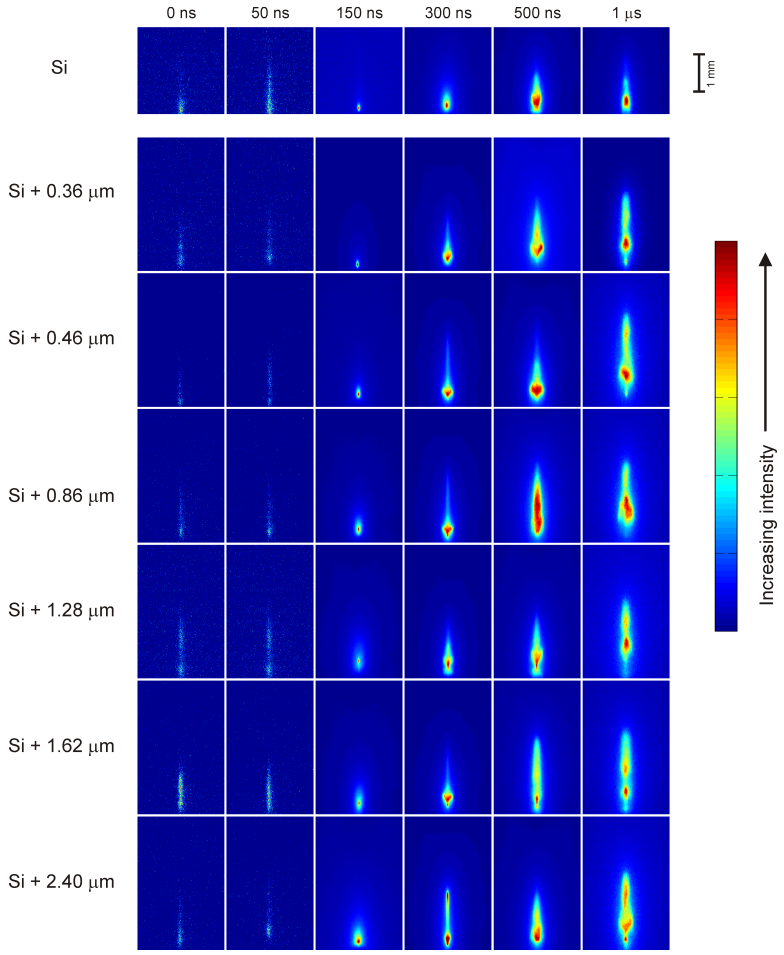

Figure 4.6: Time resolved ICCD images of plasma induced on bare silicon and silicon with a thin film deposited on its surface. The film thickness ranges from 0.36 μm to 2.40 μm. Delay times represented are 0, 50, 150, 300, 500 ns and 1 μs. The color bar indicates relative intensities only within an individual plasma image; intensities between images cannot be compared.

The biggest plasma in the series is shown for the 2.40 μm film thickness. At 300 ns delay time, the plasma formed on bare silicon appears different to plasmas formed on silicon with films deposited. A channel-like jet, of plasma expansion appears in the center, producing a cooler zone. This effect is clearly accentuated in the range of thinner films (0.36-0.86 μm). In the 1.28 μm film on Silicon, the splashing of the film produces a disturbance in plasma which affects the emission even at 1 μs delay time.

Time-resolved experiments

Fig. 4.7 shows plasma parameters obtained in time resolved experiments for the ablation of thin films deposited on silicon surface for the entire range of film thickness studied. The gate delay was fixed to a 100 ns, with a variable delay time of 100 ns. Information about plasma expansion and plasma cooling can be deduced from this figure as well as a relative measure of the initial plasma energetic states.

In Figure 4.7 (A) plasma temperature is represented for each film thickness. Although, the initial energetic state in each sample is very similar, emission from the thicker films starts at a slightly lower energetic state. The rate of cooling is different in every case. The faster expansion of plasmas from the ablation of thinner films suggest a faster cooling of the plume. It also suggest that the plasma pressure may be larger at earlier times and producing a faster expansion (see Fig. 4.6 jet-like plasma). The emission from thicker films ablation comes from lower energetic state but remains at the same state last longer.

In Figure 4.7 (B) electron number density of plasmas is represented for each film thickness. The combined effect with temperature can produce plasmas with different ionization degrees. The possible plasma confinement by the films can affect to the ionization. This effect can be clearly observed looking at shorter times of 0.46 and 0.86 μm thick films, in which plasma confinement under the film yield a larger electron number density.

Parameters that can be related to a different ablation process depending on the thickness of the films are: temperature, which gives information about energetic states and plume expansion; electron number density, which gives information about the plasma ionization degree and amount of mass in plasma. These parameters are also directly related to the plasma pressure.

Different types of plasma can be considered regarding the plasma temperature and density. Particle number density of air is usually higher than particle number density from LIBS plasmas. Densities of plasmas induced by LIBS are in the range from 10^{14} to $10^{22} m^{-3}$ (by comparison, the density of air is $2.7\text{x}10^{25} m^{-3}$) [11]. Plasma is usually considered as an ideal gas. The Joule-Thomson effect on the expansion of a gas implies cooling of the gas and this cooling is faster when the gas expands faster. Plasma pressure is related to the plasma expansion at certain time. Then, by assuming plasma as an ideal gas, pressure inside of plasma can be estimated by Dalton's law:

$$P = (n_0 + n_i + n_e)kT \tag{4.2}$$

Mao et al. [42] attributed the initial decrease of number density and temperature to a fast expansion of the plasma without background gas. Authors assumed the speed of spherical plume expansion conforms with a free expansion speed. At early times, after free expansion, the expansion speed adjust to a shock wave expansion speed due to the background gas density.

Figure 4.8 shows the pressure values estimated by equation 4.2 as a function of film thickness at short delay time (100 ns). Plasma pressure is estimated to be higher when the effect of plasma confinement is higher. In the case of a plasma confined underneath a thin

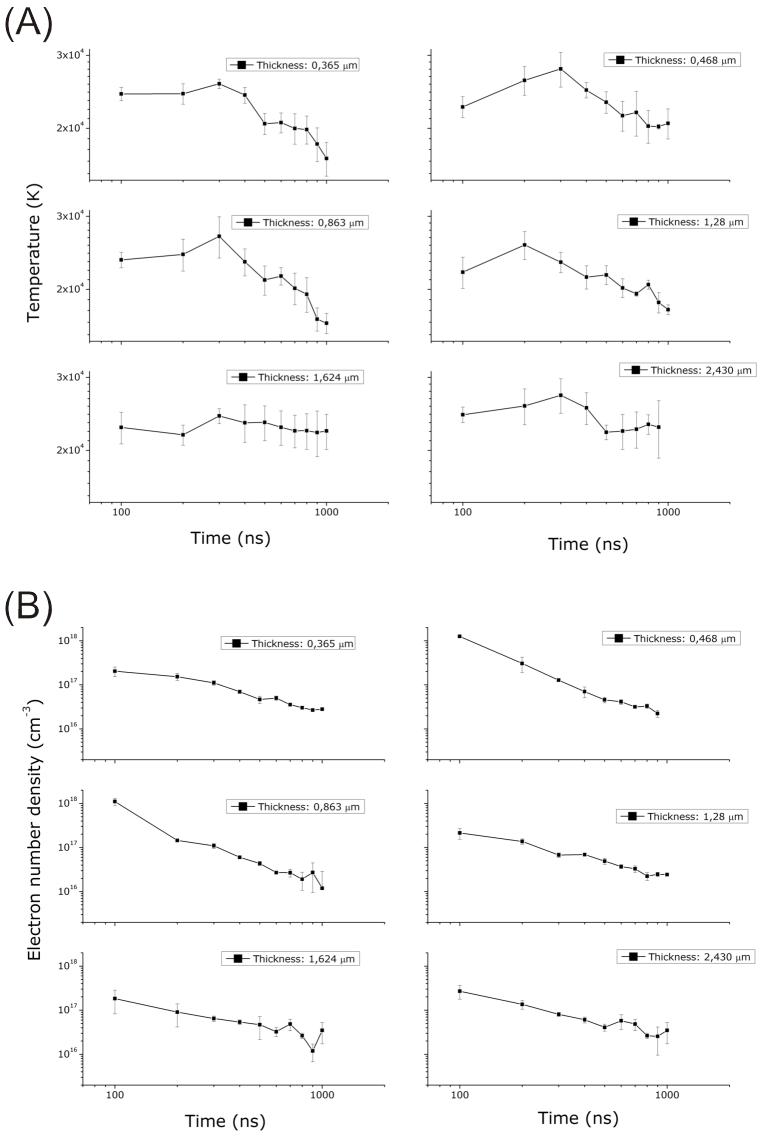

Figure 4.7: (A) Temperatures and (B) electron number density in time-resolved experiment for the whole range of film thickness under study. t = 100 ns; Δt = 100 ns

film, the plasma pressure is assumed to increase with increasing film thickness to a limit. The effect that film thickness has in plasma pressure is accentuated at short delay times.

In Fig 4.8 plasma pressure varies in a range of thickness, being higher at 0.46 and 0.86 μm of film thickness. This is because thinner films tend to produce a confinement of plasma until film spallation occurs and they do not liberate the energy easily. In the case of thicker films, even when they produce a plasma confinement they tend to liberate the energy accumulated in the form of a mechanical splashing of the films (Fig. 4.2), which dissipates energy and produces a sudden decrease in plasma pressure. In Fig. 4.8 can be seen how the weakest

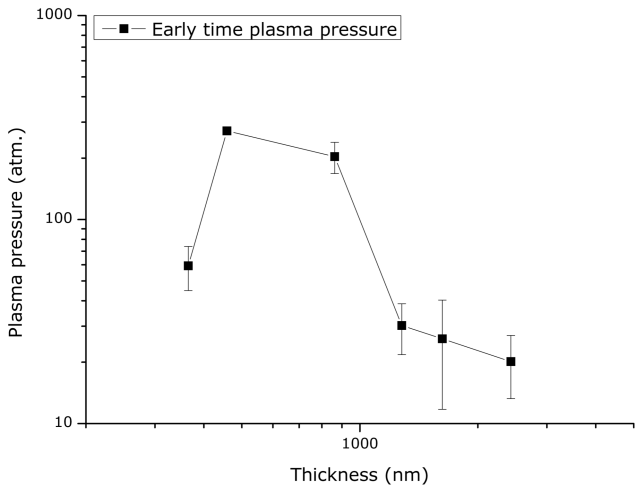

Figure 4.8: Early stages plasma pressure as a function of film thickness, calculated at 100 ns delay time.

film (0.36 μm) presents a higher plasma pressure than films in the range of 1.28-2.40 μm. In this figure can be seen how different ablation regimes of the films affect the plasma pressure.

4.5 Conclusions

Spallation of transparent organic thin films can be achieved by the ablation of silicon substrate. Three possible regimes are proposed as function of laser fluence and film thickness. These very different ablation regimes have consequences in optical emission of the plasma formed, being difficult to evaluate the amount of material in plasma that comes from thin films. These mechanisms seem to be strongly dependent on laser fluence more than in laser irradiance. It has been shown that the single shot experiments for femtosecond and nanosecond ablation gave very different results.

Imaging experiments provided information about the different shape and size of silicon plasmas when a thin film is deposited on the surface. The elongation of plasmas producing a jet in the center, which seems to expand faster and can be linked to a cooler zone and are typically formed in thinner films.

The combined effect between ablated mass and plasma temperature can be clearly seen in optical emission, where the intensities of atomic and ionic lines have different behavior as function of film thickness. While atomic emission is slightly increased at a film thickness of 1.28 μm, the ionic emission presents a decreasing emission intensity at the same point. The ionization degree of plasma is lower at higher film thickness.

The time resolved experiment revealed how the plasma expansion and plasma cooling can vary as a function of film thickness, which is coincident with imaging experiment. The faster plasma expansion can be seen in the plasma images as the formation of jet-like plasma.

Chapter 5

Depth Profiling with LIBS

5.1 Introduction

Laser induced plasmas have been used quite successfully for analyzing thin film structures, solar cells and other photovoltaic devices. LIBS has been used as a means of depth profiling and characterization for artwork, archeology, metals and coatings. The analysis of multi-layered thin films introduces key challenges to conventional LIBS. As the laser successively removes layers of material, the plasma properties and ablation efficiencies may change. This can introduce confusion in the LIBS signal unless careful attention is paid to the individual layer's ablation properties. Additionally, the typical intensity profile of a laser beam is Gaussian in shape, producing concave craters. As the laser removes more and more material, a contribution to the LIBS plasma from the sloped edges of the crater across multiple layers is common. Changing the beam shape or using a laser with a "'flat-top"' profile enhances the accuracy and resolution of the LIBS results by producing a crater with straight edges. An application of depth profiling with LIBS is the analysis and process control of CIGS solar cell production. This type of industry requires high speed analysis capable of thin film multi-layer and multi-element measurements without the need for vacuum chambers or sample preparation. While LIBS may not be able to provide the most highly accurate quantitative analysis of an unknown sample, it is ideal for process control where calibration curves can be generated and detailed elemental concentration and identification is necessary.

5.2 Beam Shaping

The depth-profiling of multi-layered structures relies heavily on the ability to remove a thin uniform layer of material. Most solid state lasers in use have a Gaussian beam profile which produces concave ablation craters. This curved profile of the crater introduces material from two or more layers in the same laser pulse. In order to minimize interference and contribution from multiple layers in the LIBS signal, the beam profile should be homogeneous and uniform intensity. In an effort to homogenize the beams, a set of telescopic non-Gaussian optics were

used in conjunction with a beam expander. In order to test the effectiveness of this system, a poorly maintained Nd:YAG (New Wave Research Tempest) at 1064nm laser was used. The raw beam profile shown in Figure 5.1(a) has a very poor Gaussian shape with localized regions of high and low intensity. This laser produces very irregular ablation craters. The modified beam profile using commercially available beam shaping optics (πShaper® 6_6_1064) is shown in Figure 5.1(b).

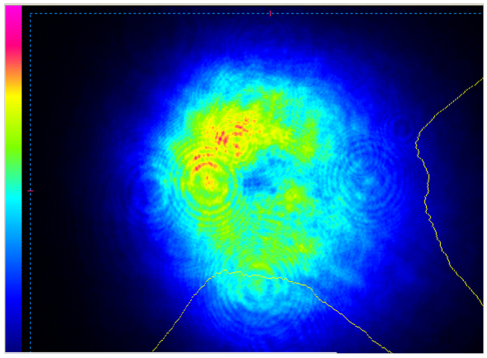

(a) Unmodified

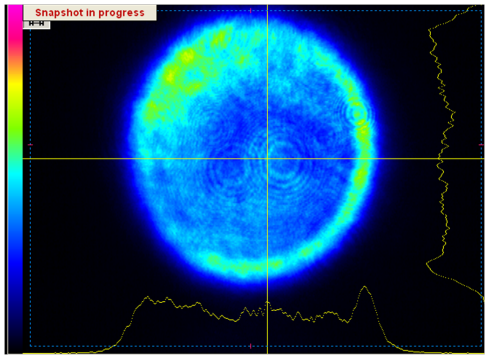

(b) Pi-shaper

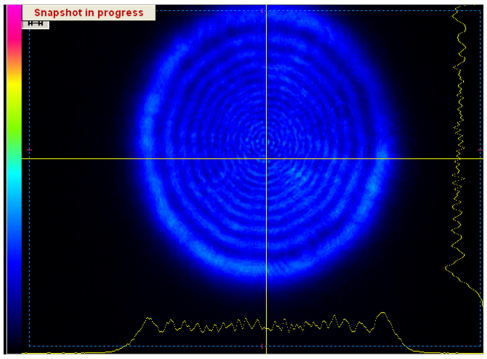

(c) Beam expander 4x

Figure 5.1: Beam profiles for the raw and modified laser output

This system required extensive initialization efforts and was very sensitive to use. Each of the two components, beam expander, and beam shaper, require the use of 5-degree of freedom optical mounts. This system made using the device very difficult. Additionally, the system did not offer any beam homogenization as seen in Figure 5.1(b). It was determined through extensive testing using a beam profilometer and actual ablation of various materials that this type of beam shaping optics did not provide a robust solution. Instead, a 10x beam expander was used in conjunction with two irises separated by 1m to select the center region of a Gaussian beam. This expander and iris combination was applied to the output from another Nd:YAG laser (New Wave Research Minilase-III) with a high quality beam

Gaussian beam profile. This combination provides a uniform nearly flat beam profile with a long focal waist, prefect for depth profiling of multi layered structures.

5.3 Crater profile analysis

In order to verify some preliminary depth profiling results using LIBS it became necessary to analyze the ablation craters in cross section. This provides a vital comparison between the the axial material removal and identification with a physical measurement of the crater and layers. The material system chosen for this test was a hard disk platter for a variety of reasons. The hard disk consists of a relatively thick NiP layer on an Al-alloy substrate. The Al-alloy substrates usually contain 4-5% Mg, with trace amounts of Si, Fe, Zn, and Cu. The material used to identify the substrate layer was Mg due to its strong LIBS signal. The surface and interface between layers is uniform, well defined and extremely smooth to eliminate the possible effects from morphology. During construction of the platter, the substrate is polished smooth prior to NiP plating which is then polished to a surface roughness of less than 0.1nm.

Results

The hard disk was ablated using a 1064nm laser passing through a 10x beam expander, 2 irises, and a 3x focusing objective lens. The LIBS signal was collected and analyzed using a broadband CCD spectrometer. Several lines of ablation craters were made at 40, 60, 80, and 100 shots. The platters were then diced and mounted vertically in epoxy casting resin. The resin blanks were then polished down with coarse 120-grit polishing discs until the craters became visible in the microscope. The polishing of the mounted samples was adjusted by hand until the cross-section of the crater was centered. The samples were then polished with progressively smoother grinding disks and finished with a 0.03μm polishing compound. The optical microscope images are shown in Figure 5.2.

The LIBS signal was collected for a series of 200 shots in order to ensure complete removal of the NiP layer. The Ni and Mg signals shown in Figure 5.3 are associated with the series of 200 shots at 50mJ and 60mJ laser pulse energies. The cross-over point, or interface for the 60mJ case shown in Figure 5.3(b) occurs at roughly 80 shots. That crater was analyzed with a scanning electron microscope in order to determine exactly how the transition between NiP layer and the Al-alloy occurs. The image appears to show penetration into the Al-alloy occurring at the edge of the crater. This indicates that the beam shaping technique is working and the beam profile is relatively uniform and flat. The ablation properties of the two materials are different, and the effect can be seen in Figure 5.2(d). Once the Al-alloy layer is reached, a much more aggressive ablation takes place with a higher degree of hydrodynamic splashing. The Al material is spread up and begins to coat the NiP edges of the crater. This provides an ideal example of a case where tailoring the ablation parameters (wavelength,

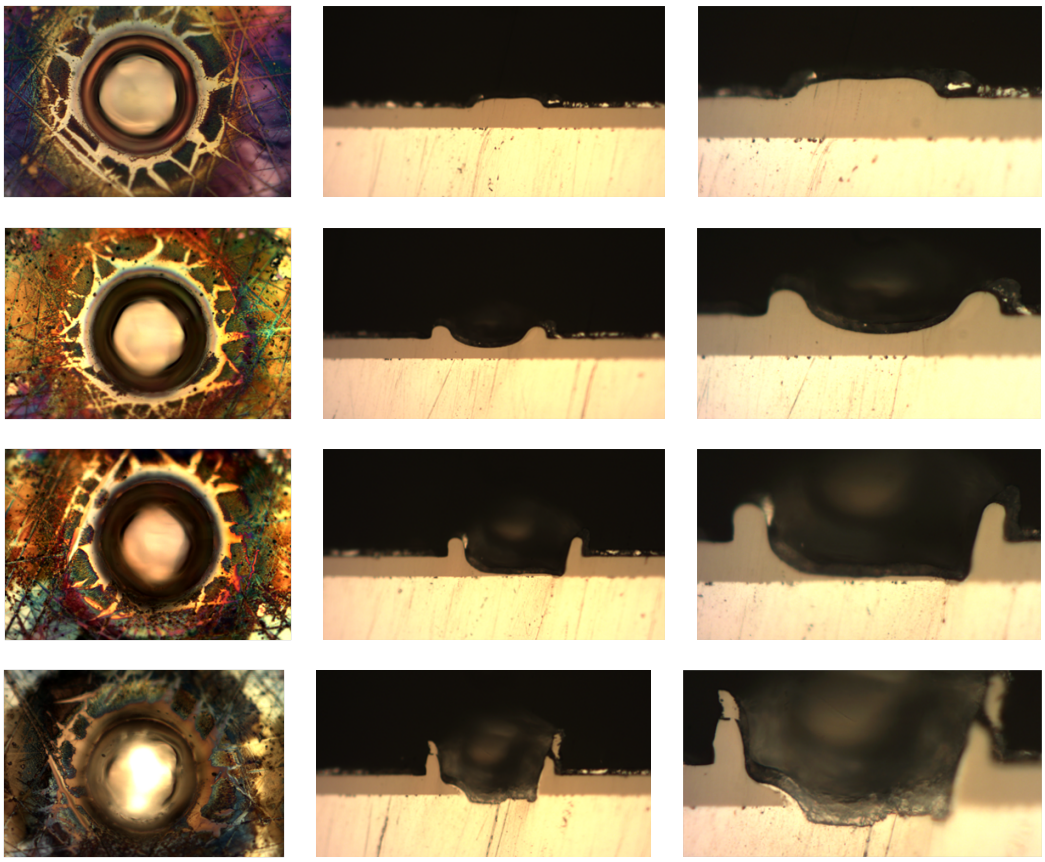

Figure 5.2: Ablation craters and cross-sections for (a) 40 shots, (b) 60 shots, (c) 80 shots, and (d) 100 shots with 60mJ laser pulses

laser energy, beam size etc.) to the individual layers would improve the resolution and quality of the depth profiling.

5.4 Depth profiling of CIGS solar cells

In recent years the focus on energy research has gained more popularity and much more funding, both private and federal. A multitude of companies have started producing different types of solar cells in the race for efficient affordable solutions. One such solution is the CIGS solar cell which can be produced in roll-to-roll printed fashion. LIBS provides and ideal analysis and quality control solution for this type of industry. The ability to conduct detailed multi-layer analysis at high volume production speeds is one unique to laser-based spectrometry.

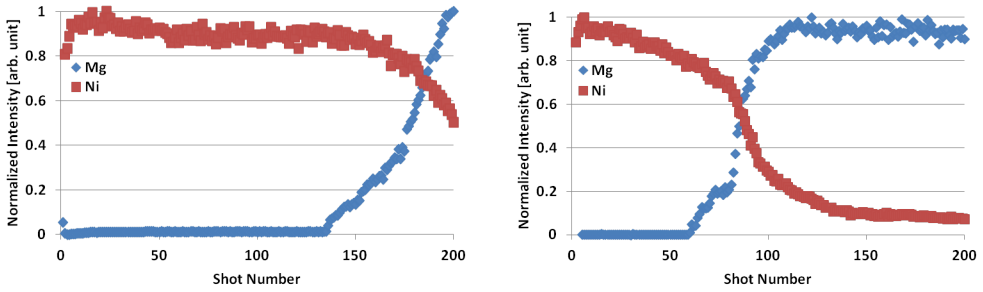

(a) 50mJ (b) 60mJ

Figure 5.3: LIBS results for ablation of hard disk platter

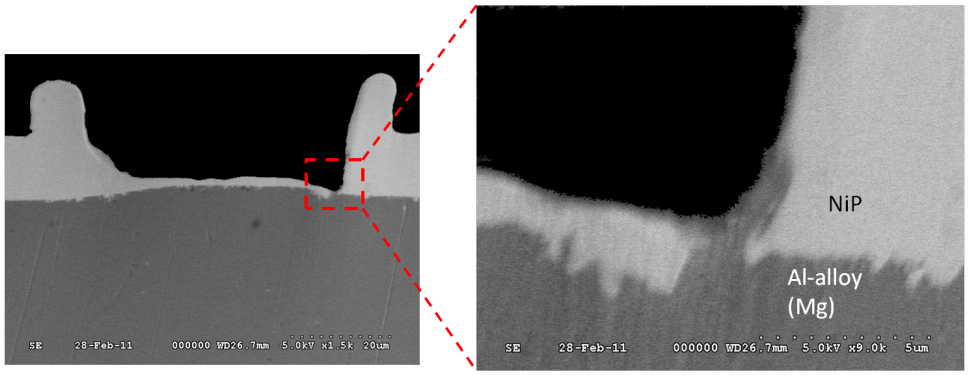

Figure 5.4: Scanning electron micrograph of laser ablated hard disk from 80 shots at 60mJ

CIGS Precursor Material LIBS

Conducting detailed depth profile analysis of multi layered materials can be aided by understanding the ablation properties of the individual layers. An ablation study was conducted of bulk Cu, In, and Ga to investigate any difference in ablation threshold. Each material was mounted in casting resin and polished to 1200-grit and then cleaned with acetone, isopropyl alcohol, and distilled water. The samples were then ablated with 1064nm, 532nm, and 213nm at various laser energies. The ablation craters were then analyzed with a white light interferometer and the diameters and depths recorded. The square of the diameter was then plotted as a function of laser fluence and the results are shown in Figure 5.5.

It has been determined that the ablation threshold of each material is very similar and does not vary significantly with laser wavelength. The ablation of the CIGS layer on a solar cell should occur uniformly assuming the laser fluence is significantly higher than the ablation threshold.

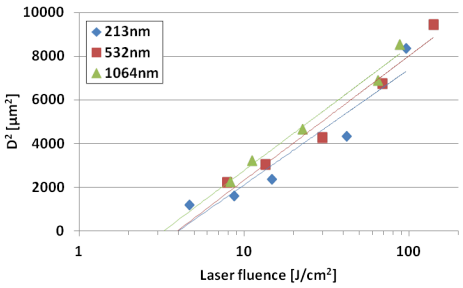

(a) Cu

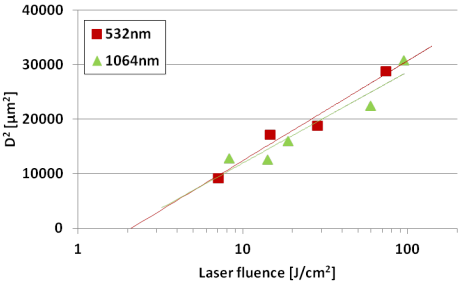

(b) In

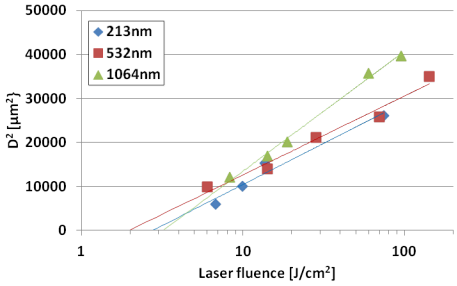

(c) Ga

Figure 5.5: Ablation threshold analysis for CIGS precursor materials

Table 5.1: Measured ablation threshold of bulk Cu, In and Ga

Material	Ablation Threshold (J/cm^2)
Cu	3.7
In	2.0
Ga	2.5

CIGS Depth Profiling Results

A roll-to-roll CIGS solar cell printed on an aluminum substrate was analyzed with LIBS using an Nd:YAG laser (Quantel Brilliant) at 1064nm, 532nm, and 266nm wavelengths. The typical construction of this cell is shown in Figure 5.6. The exact composition of the CIGS layer was kept confidential by the sample supplier, however the general construction is known and there is a gradient in In concentration through the CIGS layer. The laser induced plasma optical emission was collected using quartz imaging optics onto a fiberoptic cable. The spectra was analyzed with a symmetrical Czerny-Turner CCD broadband spectrometer (Avantes AvaSpec-2048x14 Fiber Optic Spectrometer) with a typical resolution of 0.1nm. The plasma emission from each laser pulse was collected and analyzed, extracting the relevant information for each elemental system. The normalized LIBS signals for each element at each

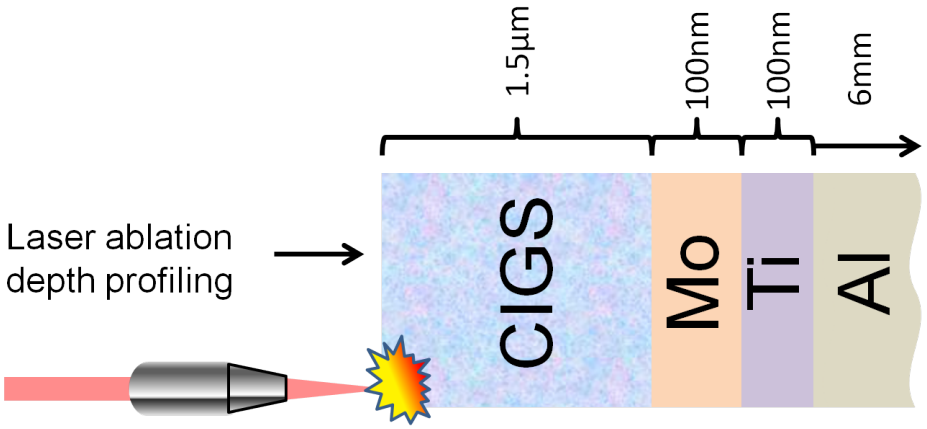

Figure 5.6: Typical construction of roll-to-roll printed CIGS solar cell on aluminum substrate

wavelength is shown in Figure 5.7. The laser fluence for each wavelength was kept the same in order to analyze the effect of laser wavelength. In the LIBS results the Cu and Ga signals remain consistent while the In signal decays in the layer as expected for the 1064nm and 266nm results. The CIGS layer results for the 532nm test show inconsistent behavior for the Ga signal. In all three cases the Mo and Ti layer were clearly defined. The 532nm laser efficiently removed the CIGS layer in roughly 6 shots while the 1064nm and 266nm lasers required 8 and 20 shots respectively. This may be due to the design of the CIGS layer to absorb visible radiation. The 266nm laser provides a very shallow laser penetration depth and removes a thin layer of material at a time. However, the transitions between layers are not as well defined as in the 1064nm and 532nm cases.

5.5 Conclusions

The use of LIBS for depth profiling of solar cells had been shown to be an effective means to identify and monitor the material composition of these multi-layered structures. Careful attention must be paid to the beam shape and homogeneity to ensure the highest resolution analysis. In order to optimize LIBS on-the-fly, an understanding of the best ablation properties and spectral acquisition parameters is needed. Choosing the right laser wavelength and power can also help by optimizing the optical penetration depth, and ablation rate of the exposed material layer of interest. The use of a high power beam expander proved to be an adequate and robust solution, providing a uniform flat laser intensity profile from an originally Gaussian beam. The laser ablation of bulk CIGS materials showed no significant difference in ablation threshold or dependence on laser wavelength. The Cu, In, Ga, Mo, and Ti layers were all clearly identifiable in the LIBS signal and consistent across multiple wavelengths. The use of 266nm wavelength laser provides a lower ablation rate but less

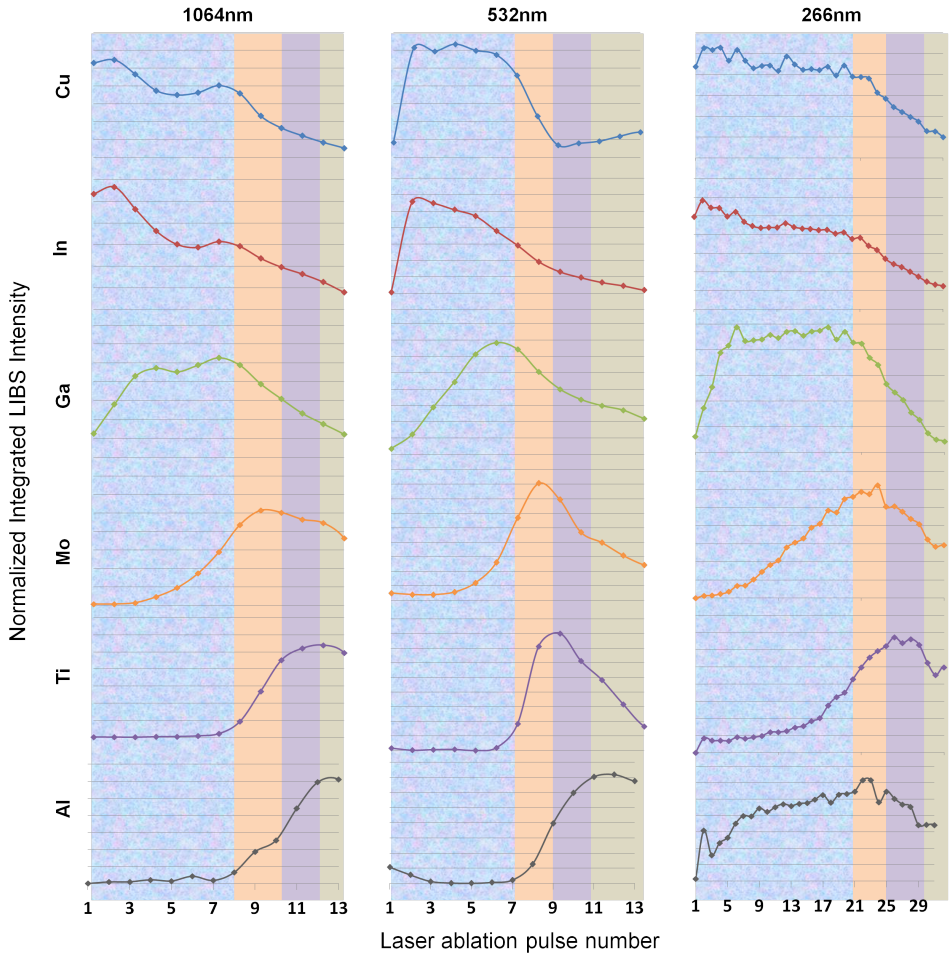

Figure 5.7: Depth profiling of CIGS solar cell using a nanosecond Nd:YAG laser at a)1064nm, b) 532 and c) 266nm wavelength

sharp transition between layers compared to the 1064nm and 532nm results.

Chapter 6

Matrix Effects in LIBS

6.1 Introduction

During the last decades laser induced plasmas have gained a deserved importance in material science. Particularly, the optical emission spectroscopy of laser induced plasmas, also known as laser induced breakdown spectroscopy or LIBS, has become a very popular analytical technique not only in solids characterization (such as art or archaeological samples [5, 28]) but also in liquids [28, 56], aerosols [53, 35] and even powder sample [28, 61] analysis. The growing interest in laser induced breakdown spectroscopy is primarily due to the simplicity of the technique, which provides a fast and reliable in-situ analysis with little to no sample preparation [52, 24, 7]. As the name LIBS implies, the measurements rely on the laser ablation of the material under study. The use of lasers as analytical tools can offer many benefits, but the measurements made are inextricably bound by the interaction between the laser energy and the sample material. This interaction is a very complex process in which the composition, morphology, and concentration of the material being ablated can affect the measurement. Due to laser-target interaction and the subsequent processes taking place throughout the plasma evolution, the measured optical emission and physical plasma properties can be affected by the overall sample composition [24, 4]. Thus, the emission line intensity detected is related to both the element of interest concentration and the surrounding sample matrix. This phenomenon known as matrix effects is one of the unresolved and not fully explained problems with LIBS as an analytical tool. Since laser induced plasmas have higher density of material than other plasma sources [24], stronger matrix effects are shown and a more comprehensive study is necessary. Previous studies have been carried out concerning matrix effects in various samples analyzed by LIBS. For instance Eppler et al. [1] studied Pb and Ba in soil and sand through the ratio of analyte signal to another element signal present in the sample matrix. The ratio $Ba(\mathrm{II})/C(\mathrm{I})$ was found to be strongly influenced by the matrix composition. It was attributed to an increase in electron density due to an easily ionizable element, that leads to an increase in electron-ion recombination and consequently to an increase in plasma neutral species. The matrix effects of Pb in sand and

soil samples were also studied by Bulatov et al [15] with both spatial and temporal resolution. In this work the authors found dependence not only with the matrix sand content but also with the acquisition distance, which is explained as geometrical matrix effects. Chemical matrix effects were also investigated in several materials, concluding that Ca, Fe and Sr are not significantly affected by the matrix content whereas Si and Al are notoriously matrix-dependent. Chaleard and co-workers [16] studied Cu emission signal in different targets and observed significant matrix effects in samples with high Zn contents. They conclude that the material vaporization seems to be dependent on the major sample element but the excitation temperature can be affected by the presence of different amounts of Zn. The acoustic signal, which is connected to the mass ablated and the temperature, was used to satisfactorily correct the matrix effects. In other work performed by Krasniker et al. [38] shock waves are also used to identify and correct matrix effects in laser induced plasmas. In this case, the author maintains that matrix effects are governed by the energy that is not taking part on the ablation process but is absorbed by the sample. On the other hand, some other works reports light or even no matrix effects in Fe, Cu, Ni or Al [3, 6, 66] laser induced plasmas. It has been shown by George Chan et. al [19] that the presence of Na, Ba, Ca, and La induce matrix effects with varying degrees. According to literature, the matrix effects on ionic lines are much stronger than the neutral or atomic lines. The ICP-AES results produced by George et. al. indicate that the strength of the plasma-related matrix effect obeys the following trend: $Na < Ca < Ba < La$. Although the induced effect will be unique to different samples, the average effect of the aforementioned matrix components is a reduction of relative ionic line intensity by 1, 16, 19, 45% respectively. This diverse response of several elements under different conditions shows the lack of clear explanation for matrix effects in laser induced plasmas, an important and yet unresolved problem of laser based techniques. Other studies have been performed in order to explain the differences found in matrix effects for diverse elements and try to find an explanation linked to their chemical properties. It has been previously shown in inductively coupled plasmas studies that matrix effects are more severe for elements which have low secondary ionization potential [17]. Chan et al. [18] carried out a complete study of plasma-related matrix effects in inductively coupled plasma optical emission spectroscopy (ICP-OES, ICP-AS) using matrices with low secondary potential. They observed that many elements matrix effects are related to their 2nd ionization potential yet some elements present an out-of-trend behavior (Ba, Sr, Ca, Yb, Sn, Pb and Ge) and that was correlated to the double charged ions low-lying energy levels. The goal of this work is to investigate laser induced plasma matrix effects of some out-of-trend elements previously observed for inductively coupled plasmas [18]. To examine this anomaly, the ionic to atomic line intensity ratio is studied as a warning indicator of plasma related matrix effects, due to its independence of the sputtered material and its sensitivity to plasma excitation changes [19].

One indicator of plasma-related matrix effects is the intensity ratio of ionic and atomic emission lines for the same element. This ratio is directly related to plasma temperature and electron number density for plasmas that are in thermodynamic equilibrium. This ratio is indicative of the plasma conditions and can be used to compare many elements. It has

also been widely used in ICP-AES both to indicate the presence of matrix effects and to verify and establish the quality of the inductively coupled plasma(JAAS 2008 George 2,13-16,18-22). Although many elements are effective indicators, the Mg II 280.270 nm to Mg I 285.215 nm line pair is one of the most widely used (JAAS 2008 George 2,13-16,18 ;J. anal. At. Spectrum 2008, 23,181-192). This pair makes an excellent indicator as the two lines are relatively close to one another and can be acquired in the same spectral window for high-resolution monochrometers. Additionally the lines are very intense and effective use requires only a small amount of Mg be present in the laser induced plasma. This technique requires that Mg be present in the samples or artificially added as a trace element. It is also important that there are no spectral interferences between the trace element and the other matrix elements.

6.2 Sample Preparation

Control over sample preparation was critical in order to determine the matrix effect in LIBS, binder/analyte interaction, and the impact on plasma properties. The samples used in this study were made using a paraffin binder (PBX1-454, VHG labs) to which varying amounts of SiO_2 powder (Alfa Aesar 99.9%) were added. In order to calculate plasma properties, a tracer material was added such that all the required emission lines lied within a single spectral window from the high resolution monochrometer. Magnesium was chosen as the tracer element and was incorporated into the prepared samples in the form of $MgCO_3$*n-hydrate(Baker 2436-01). The binder, tracer, and analyte were ball-milled using a Spex sample prep 8000M Mixer mill prior to pelletization. The first series of 5g samples were made only with binder and tracer material with an Mg concentration of 0.5%, 1.0% and 2.0%. Two samples were made of each concentration and were milled for 5min, and 10min. Preparation techniques were varied in order to determine the conditions which provide the best homogeneity, sample consistency, and signal uniformity. The milled powders were pressed into samples using a Spex 3630 x-press with a 31mm die. The die was cleaned between pressings with lubricant spray.

6.3 Results

The samples were then loaded into the LA-ICP apparatus and analyzed in the time of flight mass spectrometer. Signal variation was much lower for the samples milled for 10min, and that sample preparation procedure was chosen and used throughout subsequent experiments.

The second series of experiments were conducted to study how the addition of a second element influences the matrix effects. Additional samples were made using various amounts of $MgCO_3$ in order to generate a calibration curve for the tracer element. The 5g samples each contain binder $MgCO_3$ such that the Mg concentration was 0.5%, 1.0%, 2.0%, 4.0%, 6.0%, 8.0% and 10.0% by weight. These samples were individually loaded into the LIBS

experimental system described in previous sections and ablated with a 1064nm Nd:YAG nanosecond laser (Newwave MiniLaseIII). The beam was focused using a 5x microscope objective with a final beam spot of $80\mu\ m$.

The spectra for this preliminary study was collected and analyzed using an Avantes spectrometer with 0.1nm spectral resolution. The integrated peak intensity for Mg-lines are shown below. Carbon was chosen as an internal standard which should be observationally invariant among the samples.

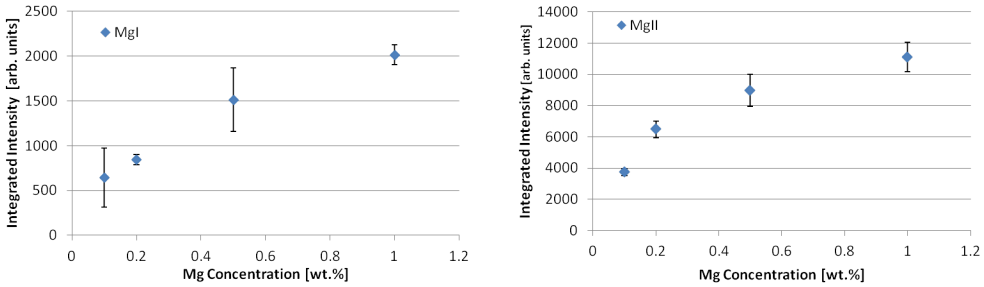

(a) Mg-I 285.21nm (b) Mg-II 280.27

Figure 6.1: Magnesium Calibration curve for $Si + Mg$ samples as a function of Mg concentration

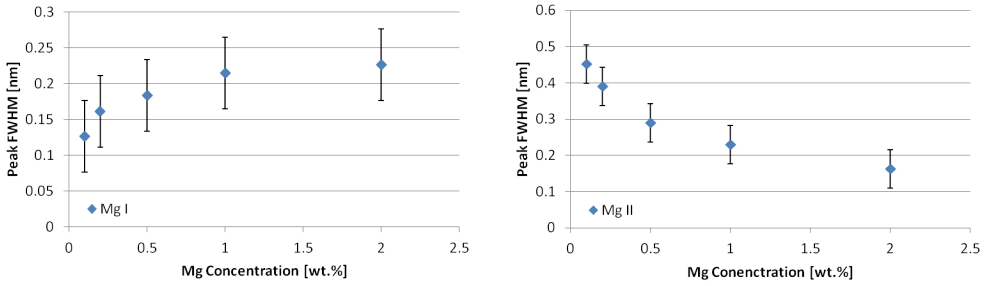

(a) Mg-I 285.21nm (b) Mg-II 280.27nm

Figure 6.2: Magnesium peak full-width-half-maximum for $Si + Mg$ samples as a function of Mg concentration

The objective of this test was to confirm that there is a linear fit to the calibration curve and to choose a concentration of Mg that would perform well as a tracer and not saturate the detector. A concentration of 1% was chosen for all subsequent samples.

The next set of samples were produced with varying Ca concentration. As seen in Figure 6.4(a), the ratio of $MgII/MgI$ decreases by maximum of 40%. This indicates a significant change in plasma properties, and verifies a Ca induced matrix effect. The calibration curve

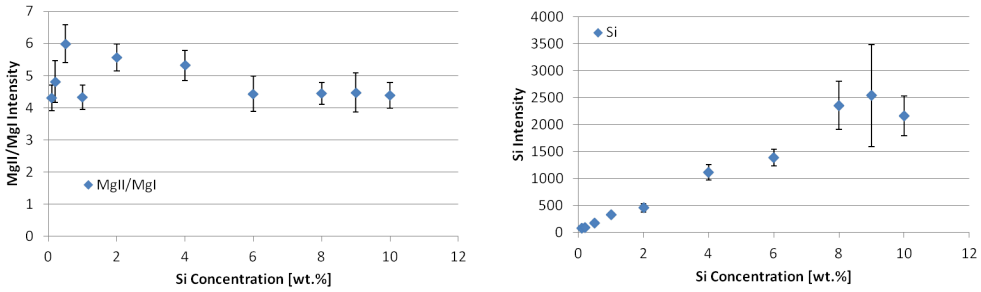

(a) MgII/MgI (b) Si

Figure 6.3: Magnesium peak ratio and Si calibration curve intensities for $Mg + Si$ samples as a function of Ca concentration

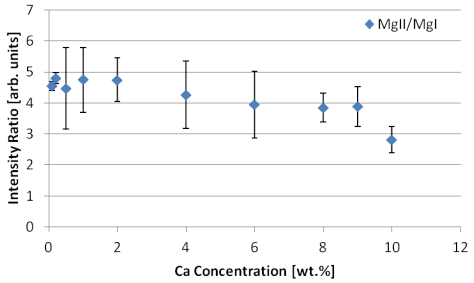

(a) Mg-II / Mg-I

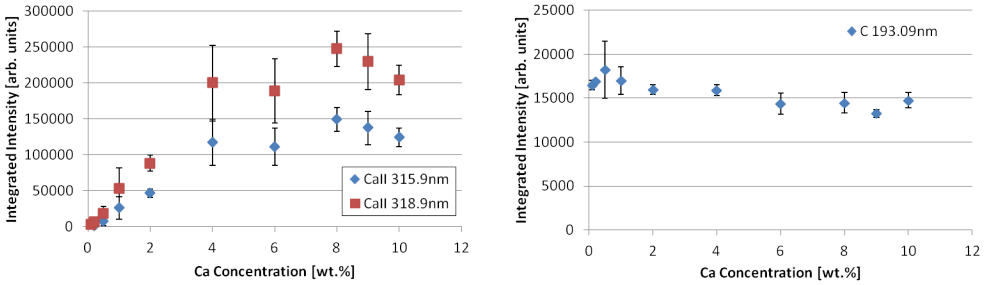

(b) Ca-II (c) C

Figure 6.4: Magnesium peak ratio, Ca-II and C-I integrated intensities for $Mg+Ca$ samples as a function of Ca concentration

generated in Figure 6.4(b) shows a generally increasing trend, however the variability in the data is much higher than desired. Additionally the data points do not show a smooth trend. The figure indicates the possibility of a saturation, or roll-off in the calibration curve at a concentration grater than 8% and the experimental data should be limited to the linear portion of the curve. The C integrated intensity in Figure 6.4(c) remains relatively flat

across the various Ca conentrations. This is used as an internal standard and is the main constituent of the matrix material.

Samples were prepared with a Mg tracer and a matrix with varying concentration of Sr. The samples were then ablated using the same experimental setup and laser conditions. The

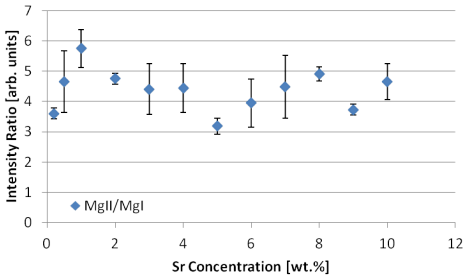

(a) Mg-II / Mg-I

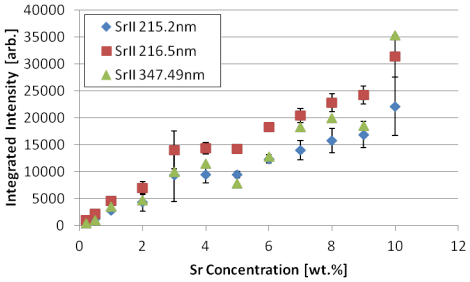

(b) Sr-II

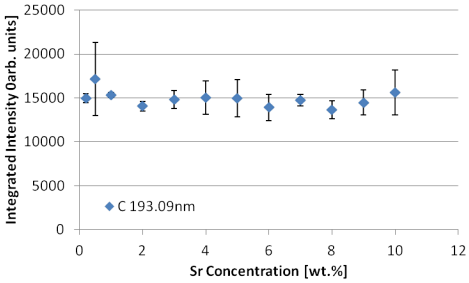

(c) C

Figure 6.5: Magnesium peak ratio, $Sr - II$ and $C - I$ integrated intensities for $Mg + Sr$ samples as a function of Sr concentration

data shown in Figure 6.5(a) indicates a high degree of variability in the ionic-atomic ratio of the Mg signal. Unfortunately there is far too much error in the data to draw any conclusions about the presence of matrix effects. The general trend of the data seems relatively flat across the different concentrations of Sr. The calibration curve shown in Figure 6.5(b) shows good linearity and low degree of error across three different emission lines. The internal standard C signal is also relatively uniform with a low degree of variability as seen in Figure 6.5(c).

6.4 Conclusions

The presence of matrix effects in LIBS is a very important problem to understand and address as further progress towards a robust qualitative measurement technique is made. It has been sown that some elements in a matrix can greatly effect the constant signal of interest. Ca showed a significant impact on the emission of Mg and should be handled carefully in any

quantitative study. At the end of this study it was determined that the laser energy used was too high. A lower ablation fluence produces a much more stable plasma and emission signal. This study should be repeated in the future with a lower energy in order to establish the plasma parameters and impact of matrix effects with more confidence.

Chapter 7

Conclusion

The goal of this dissertation was to explore the ability and effectiveness of laser induced breakdown spectroscopy to analyze thin films for a variety of applications. An introduction to LIBS as well as the components involved has been presented. The background information on plasma properties and atomic ionic emission has also been given to supplement the experimental sections.

Chapter 2 details the development of a laboratory LIBS system with the ability to utilize many different lasers, spectrometers and detectors. The sample manipulation, laser control, spectrometer control, and laser focusing has been automated to reduce the possibility of operator error. This system utilizes computer controlled equipment integrated with a custom software written in LabVIEW. The auto-focusing routine has provided tremendous improvements over manual stage control allowing a much higher throughput of samples and scanning over irregular surfaces. One of the drawbacks to this subsystem is the lack accurate focusing for ultra smooth samples. The computer controlled delay generator is the heart of the system providing accurate timing between the laser, shutter, and spectrometer.

Chapter 3 investigated the ability of nanosecond and femtosecond lasers to detect metallic impurities of titanium dioxide thin films. A series of experiments were conducted with different laser pulse durations, wavelengths and varying film thickness and dopant concentrations. This set of experiments helped determine the optimal timing of gate width and delay. This information was critical for measuring small impurities in a noisy background signal like Ti emission. A concentration of 60ppm Mg was detected efficiently in a noisy background of $TiO2$.

Chapter 4 focused on the intriguing problem of ablating transparent organic films on highly absorbing substrates. Several ablation regimes were determined with unique ablation plume characteristics which effect plasma emission and LIBS signal. Increased signal from the organic films came from thinner samples due to the effective entrainment of material in the plasma. Ablation of thicker films trapped the plasma between layers and exfoliated the film without efficiently ablating it and introducing material into the plasma. The measured plasma temperature and ablated mass were strongly correlated with LIBS signal.

Chapter 5 took the ablation and analysis of thin films to the next level by conducting

depth profile studies on multilayered solar cells. Some of the traditional challenges of laser depth profiling were addressed by modifying the beam intensity profile, and using the automated sample manipulation. The precursor materials used in the solar cell were analyzed for ablation threshold independently. Three laser wavelengths were used and 266nm produced a lower ablation rate, but 532nm produced sharper transitions between layers. Multiple layers were easily distinguished as well as elemental concentration gradients within layers. This demonstrates and ideal application for LIBS in industry where high production volumes, speed, and flexibility of analysis is critical.

In the final chapter, one of the major challenges in LIBS was explored. A series of experiments were conducted utilizing an inert base material with a tracer element and increasing quantities of elements suspected of causing matrix effects. Calibration curves were made for each material under analysis and the matrix effect indicator, $Mg - II/Mg - I$ ratio, successfully detected changes in plasma properties. The results for for matrices with Ca inclusion indicated a potential reduction in the ionic/atomic ratio of 40%. However, this result proved to be inconclusive due to the amount of variation in emission signal from other samples such as Sr samples. It is clear that more work needs to be done utilizing a lower laser fluence.

Laser induced breakdown spectroscopy is a wonderful analytical tool with a seemingly endless potential applications. It must be said that LIBS is not a complete solution and cannot be applied to universally to all analytical chemistry applications. The accuracy of LIBS as a universal measurement for all samples is still lacking but the ability to tailor the technology for specific applications with specific goals is unprecedented. In the past, LIBS was marketed as an unbiased and generic measurement technique. In practice the complexity of the processes involved is so significant that great care must be taken to develop a controlled and repeatable sequence of measurements. LIBS will continue to grow as a technology and slowly make its way into further into industry. It is my strong belief that one day more and more LIBS devices will be seen at research labs, ports of entry, military convoys, and factories with hand held devices in the tool bags of archaeologists, historians, inspectors, and investigators.

References

[1] Donald D. Hickmott Monty J. Ferris Aaron S. Eppler, David A. Cremers and Aaron C. Koskelo. Matrix effects in the detection of pb and ba in soils using laser-induced breakdown spectroscopy. *Appl. Spectrosc.*, 9:1175–1181, 1996.

[2] B. Adela and R. Byer. Femtosecond laser ablation properties of borosilicate glass. *J. of Appl. Phys.*, 96:5316–5323, 2004.

[3] J.A. Aguilera, C. Aragn, V. Madurga, and J. Manrique. Study of matrix effects in laser induced breakdown spectroscopy on metallic samples using plasma characterization by emission spectroscopy. *Spectrochimica Acta Part B: Atomic Spectroscopy*, 64(10):993 – 998, 2009.

[4] Jos F Alcntara, Jos M. Vadillo, and J. Javier Laserna. Experimental variables and matrix effects associated with the onset of ion generation in laser ionization of solid samples. *J. Anal. At. Spectrom*, 25:1424–1431, 2010.

[5] Demetrios Anglos. Laser-induced breakdown spectroscopy in art and archaeology. *Applied Spectroscopy*, 55:186A–205A, 2001.

[6] Jess M. Anzano, Mark A. Villoria, Antonio Ruz-Medina, and Roberto J. Lasheras. Laser-induced breakdown spectroscopy for quantitative spectrochemical analysis of geological materials: Effects of the matrix and simultaneous determination. *Analytica Chimica Acta*, 575(2):230 – 235, 2006.

[7] C. Aragn and J.A. Aguilera. Characterization of laser induced plasmas by optical emission spectroscopy: A review of experiments and methods. *Spectrochimica Acta Part B: Atomic Spectroscopy*, 63(9):893 – 916, 2008.

[8] N Arnold, J. Gruber, and J. Heitz. Spherical expansion of the vapor plume into ambient gas: and analytical model. *Applied Physics A: Materials Science & Processing*, 69:S87–S93, 1999.

[9] T. Asahi, H.Y. Yoshikawa, M. Yashiro, and H. Masuhara. Femtosecond laser ablation transfer and phase transition of phthalocyanine solids. *Appl. Surf. Sci.*, 197-198:555–560777–781, 2002.

[10] S. Baudach, J Bons, J Kriger, and W. Kautek. Ultrashort pulse laser ablation of polycarbonate and polymethylmethacrylate. *Appl. Surf. Sci.*, 154-155:555–560, 2000.

[11] P. M. Bellan. *Fundamentals of Plasma Physics*. Cambridge.

[12] A. Bogaerts and Z. Chen. Effect of laser parameters on laser ablation and laser-induced plasma formation: A numerical modeling investigation. *Spectrochimica Acta Part B*, 60:1280–1307, 2005.

[13] A. Bogaerts, Z. Y. Chen, R. Gijbels, and A. Vertes. *Spectrochimica Acta Part B*, 58:1867, 2003.

[14] D. N. Bose. Laser ablation of semiconductor thin films dependence of deposition rate on bandgap. *Current Science*, 42:74–83, 2002.

[15] Valery Bulatov, Rivie Krasniker, and Israel Schechter. Study of matrix effects in laser plasma spectroscopy by combined multifiber spatial and temporal resolutions. *Analytical Chemistry*, 70(24):5302–5311, 1998.

[16] C. Chaleard, Andre N. Mauchien, P. and, J. Uebbing, J. L. Lacour, and C. Geersten. Correction of matrix effects in quantitative elemental analysiswith laser ablation optical emission spectrometry. *J. Anal. At. Spectrom*, 12:183–188, 1997.

[17] George C.-Y. Chan, Wing-Tat Chan, Xianglei Mao, and Richard E. Russo. Investigation of matrix effects in inductively coupled plasma-atomic emission spectroscopy using laser ablation and solution nebulization effect of second ionization potential. *Spectrochimica Acta Part B: Atomic Spectroscopy*, 56(1):77 – 92, 2001.

[18] George C.-Y. Chan and Gary M. Hieftje. Investigation of plasma-related matrix effects in inductively coupled plasma-atomic emission spectrometry caused by matrices with low second ionization potentialsidentification of the secondary factor. *Spectrochimica Acta Part B: Atomic Spectroscopy*, 61(6):642 – 659, 2006.

[19] George C.-Y. Chan and Gary M. Hieftje. Warning indicators for the presence of plasma-related matrix effects in inductively coupled plasma-atomic emission spectrometry. *J. Anal. At. Spectrom.*, 23(2):181–192, 2008.

[20] K. Chen, R. Leboeuf, R. Wood, D. Geohegen, J. Donato, C. Liu, and A. Puretzky. Laser solid interaction and dynamics of laser-ablation materials. *Applied Surface Science*, 96-98:45–49, 1996.

[21] D. A. Cremers. The analysis of metals at a distance using laser-induced breakdown spectrocroscopy. *Appl. Spectrosc.*, 41:572–578, 1987.

[22] D. A. Cremers and L. J. Radziemski. Direct detection of beryllium on filters using the laser spark. *Appl. Spectrosc.*, 39:57–60, 1985.

[23] D. A. Cremers, L. J. Radziemski, and T.R. Loree. Spectrochemical analysis of liquids using the laser spark. *Appl. Spectrosc.*, 38:721–726, 1984.

[24] David A. Cremers and Leon J. Radziemski. *Handbook of Laser-Induced Breakdown Spectroscopy*. John Wiley and Sons, Ltd., 2006.

[25] R. Fardel, M. Nagel, F. Nuesch, T. Lippert, and A. Wokaun. Fabrication of organic light-emitting diode pixels by laser-assisted forward transfer. *Applied Physics Letters*, 91:061103–1–061103–2, 2007.

[26] R. Fardel, M. Nagel, F. Nuesch, T. Lippert, and A. Wokaun. Laser-induced forward transfer of organic led building blocks studied by time-resolved shadowgraphy. *J. Phys. Chem.*, C 114:5617–5636, 2010.

[27] C. Garca, J. Vadillo, S. Palanco, J. Ruiz, and J. Laserna. Comparative analysis of layered materials using laser-induced plasma spectroscopy (lips) and laser-ionization tome-of-flight mass spectrometry (li-tofms). *Spectrochimica Acta Part B*, 56:923–931, 2001.

[28] Rosalba Gaudiuso, Marcella DellAglio, Olga De Pascale, Giorgio S. Senesi, and Alessandro De Giacomo. Laser induced breakdown spectroscopy for elemental analysis in environmental, cultural heritage and space applications: A review of methods and results. *Sensors*, 10(8):7434–7468, 2010.

[29] H. R. Griem. *Spectral Line Broadening by Plasmas*. New York: Academic Press, 1974.

[30] H. R. Griem and R. H. Lovberg. *Plasma Physics*. Academic Press, 1970.

[31] C.P. Grigoropoulos. *Transport in Laser Microfabrication*. Cambridge, 2009.

[32] M. Han, Y. Gong, J. Zhou, C. Yin, F. Song, N. Muto, T. Takiya, and Y. Iwata. Plume dynamics during film and nanparticles deposition by pulsed laser ablation. *Physics Letters A*, 302:182189, 2002.

[33] G. Heise, M. Englmaier, C. hellwig, T. Kuznicki, S. Sarrach, and H. P. Huber. Laser ablation of thin molybdenum films on transparent substrates at low fluences. *Appl Phys A*, 102:173–178, 2011.

[34] A. Hertwig, S. Martin, J. Krger, and W. Kautek. Interaction area dependence of the ablation threshold of ion-doped glass. *Thin Solid Films*, pages 453–454, 2004.

[35] John D. Hybl, Gregg A. Lithgow, and Steven G. Buckley. Laser-induced breakdown spectroscopy detection and classification of biological aerosols. *Appl. Spectrosc.*, 57:1207–1215, 2003.

[36] H. Kim, C. M. Gilmore, J. S. Horwitz, A. Pique, H. Murata, G. P. Kushto, R. Schlaf, Z. H. Kafafi, and D.B. Chrisey. Transparent conducting aluminum-doped zinc oxide thin films for organic light-emitting devices. *Applied Physics Letters*, 76, 3:259–261, 2000.

[37] J. Kim and S. Na. Metal thin film ablation with femtosecond pulsed laser. *Opt. Laser Technol.*, 39:1443–1448, 2007.

[38] Rivie Krasniker, Valery Bulatov, and Israel Schechter. Study of matrix effects in laser plasma spectroscopy by shock wave propagation. *Spectrochimica Acta Part B: Atomic Spectroscopy*, 56(6):609 – 618, 2001.

[39] M. Lenzer, J. Kruger, S. Sartania, Z. Cheng, C. Spielmann, G. Mourou, W. Kautek, and F. Krausz. Femtosecond optical breakdown in dielectrics. *Phys. Rev. Lett.*, 80:4076–4079, 1998.

[40] H. Liu, X. Mao, J. Yoo, and R. Russo. Early phase laser induced plasma diagnostics and mass removal during single-pulse laser ablation of silicon. *Spectrochimica Acta Part B*, 54:1607–1624, 1999.

[41] S.S. Mao, F Quere, S. Guiazard, X. Mao, R. Russo, G. Petite, and P. Martin. Dynamics of femtosecond laser interactions with dielectrics. *Applied Physics A: Materials Science & Processing*, 79(7):1695–1709, November 2004.

[42] X. Mao, X. Zeng, S-B Wen, and R. Russo. Time-resolved plasma properties for double pulsed laser-induced breakdown spectroscopy of silicon. *Spectrochimica Acta Part B*, 60:960–967, 2005.

[43] X. L. Mao and R. E. Russo. *Applied Physics A*, 64, 1997.

[44] K. Meissner, T. Lippert, A. Wokaun, and D. Guther. Analysis of trace metals in comparison of laser-induced breakdown spectroscopy with la-icp-ns. *Thin Solid Films*, 453-454:316–322, 2004.

[45] A. Miziolek, V. Palleschi, and I. Schechter. *Laser-Induced Breakdown Spectroscopy (LIBS) Fundamentals and Applications*. Cambridge, 2006.

[46] H. Moenke and L. Moenke-Blankenburg. *Laser Microspectrochemical Analysis*. A. Hilger, Londond and Crane, Russak and Co., New York, 1973.

[47] L. Moenke-Blankenburg. *Laser Micro Analysis*. John Wiley and Sons, Ltd., 1989.

[48] Y. Nakata, T. Okada, and M. Maeda. Micromachining of a thin film by laser ablation using femtosecond laser with masks. *Opt. Laser Eng.*, 42:389–393, 2004.

[49] B.K.A. Ngoi, Venkatakrishnam K, E.N.L. Lim, B. Tan, and L.H.K. Koh. Effect of energy above laser-induced damage thersholds in the micromachining of silicon by femtosecond pulse laser. *Opt. Laser Eng.*, 35:361–369, 2001.

[50] T. Okada, Y. Nakata, and M. Maeda. Diagnostics of particle dynamics during optically functional thin-film deposition by laser ablation. In *Focused on Laser Precision Microfabrication (LPM 2002) RIKEN Review No. 50*. 2002.

[51] L. J. Radziemski and T.R. Loree. Laser-induced breakdown spectroscopy: time-resolved spectrochemical applications. *Plasma Chem. Plasma Proc.*, 1:281–293, 1981.

[52] Leon J. Radziemski and David. A. Cremers. *Laser-Induced Plasmas and Applications*. Marcel Dekker, Inc., 1989.

[53] Leon J. Radziemski, Thomas R. Loree, David A. Cremers, and Nelson M. Hoffman. Time-resolved laser-induced breakdown spectrometry of aerosols. *Analytical Chemistry*, 55(8):1246–1252, 1983.

[54] R. Russo, X. Mao, H. Liu, J. Gonzalez, and S. S. Mao. Laser ablation in analytical chemistry review. *Talanta*, 57:425–451, 2002.

[55] R. Russo, X. L. Mao, H Liu, J. Yoo, and S. S. Mao. Time-resolved plasma diagnostics and mass removal during single-pulse laser ablation. *Applied Physics A: Materials Science & Processing*, 69:S887–S894, 1999.

[56] Ota Samek, Dave C. S. Beddows, Jozef Kaiser, Sergei V. Kukhlevsky, Miroslav Lika, Helmut H. Telle, and Jim Young. Application of laser-induced breakdown spectroscopy to in situ analysis of liquid samples. *Opt. Eng.*, 39:2248, 2000.

[57] T. Schwarz-Selinger, David G. Cahill, S.-C. Chen, S.-J. Moon, and C. P. Grigoropoulos. Micron-scale modifications of *si* surface morphology by pulsed-laser texturing. *Phys. Rev. B*, 64(15):155323, Sep 2001.

[58] J. Singh and S. Thakur, editors. *Laser-Induced Breakdown Spectroscopy*. Elsevier, 2007.

[59] Greg P. Smestad and Michael Gratzel. Demonstrating electron transfer and nanotechnology: A natural dye-sensitized nanocrystalline energy converter. *J. Chem. Ed.*, 75:752–756, 1998.

[60] N. R. Sottos, S Kanula, and P. Geubelle. Crack initiation in ultra thin patterned films. In *11th International Conference on Fracture*, 2005.

[61] T. Stehrer, Praher B., R. Viskup, J. Jasik, H. Wolfmeir, E. Arenholz, J. Heitz, and J. D. Pedarnig. Laser-induced breakdown spectroscopy of iron oxide powder. *J. Anal. At. Spectrom*, 24:973–978, 2009.

[62] Y. Talmi. Multichannel image detectors. In *ACS Symp., Series No. 102*, 102, Washington, D.C., 1983. ACS.

[63] A. P. Thorne. *Spectrophysics*. Chapman and Hall, 1974.

[64] K. Venkatakrishnam, B. Tan, and B.K.A. Ngoi. Femtosecond pulsed laser ablation of thin gold film. *Opt. Laser Technol.*, 34:199–202, 2002.

[65] F. Vidal, S. Laville, B. Le Degoff, T. Johnston, M. Chaker, O. Barthelemy, J. Margot, and M. Sabasai. Annual meeting of osa - optical society of america, 2001.

[66] Jens Vrenegor, Reinhard Noll, and Volker Sturm. Investigation of matrix effects in laser-induced breakdown spectroscopy plasmas of high-alloy steel for matrix and minor elements. *Spectrochimica Acta Part B: Atomic Spectroscopy*, 60(7-8):1083 – 1091, 2005.

[67] J. Wang, R. L. Weaver, and N. R. Sottos. A parametric study of laser induced thin film spallation. *Experimental Mechanics*, 42:74–83, 2002.

[68] X.C. Wang, G.C. Lim, H.Y. Zheng, F.L. Ng, W. Liu, and S.J. Chua. Femtosecond pulse laser ablation of sapphire in ambient air. *Appl. Surf. Sci.*, 228:221–226, 2004.

[69] X. Zeng, X. Mao, and R. Greif. Experimental investigation of ablation efficiency and plasma expansion during femtosecond and nanosecond laser ablation of silicon. *Appl. Phys. A.*, 80:237–241, 2005.